Received: 14 October 2020 | Revised: 8 November 2021 | Accepted: 18 November 2021

DOI: 10.1002/hipo.23402

RESEARCH ARTICLE

WILEY

Plasticity impairment exposes CA3 vulnerability in a hippocampal network model of mild traumatic brain injury

Samantha N. Schumm[1] | David Gabrieli[1] | David F. Meaney[1,2]

[1]Department of Bioengineering, School of Engineering and Applied Sciences, University of Pennsylvania, Philadelphia, Pennsylvania, USA

[2]Department of Neurosurgery, Penn Center for Brain Injury and Repair, Perelman School of Medicine, University of Pennsylvania, Philadelphia, Pennsylvania, USA

Correspondence
David F. Meaney, Department of Bioengineering, School of Engineering and Applied Sciences, University of Pennsylvania, Philadelphia, PA, USA.
Email: dmeaney@seas.upenn.edu

Funding information
National Institute of Neurological Disorders and Stroke, Grant/Award Number: NS088176; Paul G. Allen Frontiers Group, Grant/Award Number: 12347

Abstract

Proper function of the hippocampus is critical for executing cognitive tasks such as learning and memory. Traumatic brain injury (TBI) and other neurological disorders are commonly associated with cognitive deficits and hippocampal dysfunction. Although there are many existing models of individual subregions of the hippocampus, few models attempt to integrate the primary areas into one system. In this work, we developed a computational model of the hippocampus, including the dentate gyrus, CA3, and CA1. The subregions are represented as an interconnected neuronal network, incorporating well-characterized ex vivo slice electrophysiology into the functional neuron models and well-documented anatomical connections into the network structure. In addition, since plasticity is foundational to the role of the hippocampus in learning and memory as well as necessary for studying adaptation to injury, we implemented spike-timing-dependent plasticity among the synaptic connections. Our model mimics key features of hippocampal activity, including signal frequencies in the theta and gamma bands and phase-amplitude coupling in area CA1. We also studied the effects of spike-timing-dependent plasticity impairment, a potential consequence of TBI, in our model and found that impairment decreases broadband power in CA3 and CA1 and reduces phase coherence between these two subregions, yet phase-amplitude coupling in CA1 remains intact. Altogether, our work demonstrates characteristic hippocampal activity with a scaled network model of spiking neurons and reveals the sensitive balance of plasticity mechanisms in the circuit through one manifestation of mild traumatic injury.

KEYWORDS
hippocampus, mild traumatic brain injury, network, phase coherence, plasticity impairment

1 | INTRODUCTION

Caused by a variety of mechanical impacts, traumatic brain injury (TBI) affects approximately 10 million people each year worldwide (Hyder et al., 2007), including 2.5 million annually in the United States alone (Cancelliere et al., 2017). Although advances in brain imaging technologies facilitated understanding TBI as a disease of the brain network (Stam, 2014), mild injuries generally lack detectable macroscale pathology (Bigler & Maxwell, 2012; Sours, Zhuo, et al., 2015), making these injuries challenging to diagnose. Also known as concussion, mild TBI has garnered interest in recent decades because it is highly prevalent (Blennow et al., 2016; Cancelliere et al., 2017; Martin et al., 2008), and there is growing appreciation for the potential long-term consequences of mild brain injuries (Cancelliere et al., 2017; Hiploylee et al., 2017). Since it remains difficult to predict which patients will recover completely and which will experience chronic symptoms, we still have much to learn to better diagnose and treat TBI across the spectrum of injury severity.

Learning and memory deficits after TBI are associated with dysfunction in the hippocampus (Paterno et al., 2017), a brain region situated in the temporal lobe of the human brain where it is vulnerable to injury (Kotapka et al., 1994; McAllister, 2011; Paterno et al., 2017; Raghupathi, 2004). The hippocampal formation consists of several subregions, including the dentate gyrus (DG), CA3, and CA1. The region has a complex array of inputs from and outputs to other areas of the brain. Briefly, it receives input from the entorhinal cortex and sends information downstream to the subiculum, which projects to subcortical structures (e.g., the amygdala and hypothalamus) (Canteras & Swanson, 1992; O'Mara, 2005) and areas of the medial prefrontal cortex (Jin & Maren, 2015). Through lesion and animal behavior studies, the hippocampus has been associated with spatial learning, episodic memory, and contextual conditioning (Bird & Burgess, 2008; Fanselow & Dong, 2010). In addition to behavior tests that implicate the region, the hippocampus is accessible in the rodent brain for electrophysiological investigation and benefits from an extensive morphological and molecular characterization of various cell types (Wheeler et al., 2015). The wealth of data about the hippocampus is challenging to synthesize but emphasizes the need to study and model the region as an entire circuit rather than isolated subregions.

In the context of TBI, there are many in vivo injury models that involve the hippocampus (Morales et al., 2005). This work has established that animals with hippocampal damage exhibit slower spatial learning and worse memory retention (Paterno et al., 2017). Furthermore, those behavioral deficits are associated with electrophysiological changes in the hippocampal circuitry. For instance, post-injury shifts in excitability occur in the DG (Folweiler et al., 2018; Santhakumar et al., 2001; Witgen et al., 2005) and in CA1 (Witgen et al., 2005), yet the exact mechanisms underlying these changes and how they vary across subregions are not known. Impairment of synaptic plasticity is one possibility, and plasticity deficits appear in both in vivo and in vitro models of traumatic injury (Albensi & Janigro, 2003). Specifically, many reports describe the inability to induce long-term potentiation (LTP), the persistent activation-dependent strengthening of synapses (Albensi et al., 2000; Aungst et al., 2014; Schwarzbach et al., 2006; White et al., 2017). Failure to induce LTP occurs most notably and consistently in CA1 (Cohen et al., 2007; Schwarzbach et al., 2006) and can persist at 7 days (Schwarzbach et al., 2006) up to 28 days post-injury (Aungst et al., 2014). Blast injury, often considered a milder form of TBI, can produce similar deficits in LTP (Effgen et al., 2016; Vogel et al., 2016; Vogel et al., 2017). Still, plasticity impairment remains an underexplored mechanism of mild TBI. In this work, we model the change as a modest decrement in potentiation and explore functional and structural effects.

Due to our interest in neuron- and circuit-level effects of injury, we developed and tested a computational model of the hippocampus to investigate how deficits in plasticity affect both activity patterns within subregions of the hippocampus and coupling of activity across these subregions. There are existing experimental methods (e.g., microelectrode arrays, calcium imaging, in vivo electrophysiological recording) to record this type of activity (Chen et al., 2013; Harvey et al., 2009; Lein et al., 2011), but they have shortcomings for our application. For instance, experimental models of TBI affect the entire region of the hippocampus and surrounding synaptic connections. With the sensitivity of current recording methods, it is difficult or impossible to obtain pre- and post-injury measurements. Finally, existing experimental methods offer a limited view of the entire hippocampal circuit, either lacking simultaneous measurements across all subregions or neuron-level resolution. Due to its isolated circuitry, a computational model of a single brain region contends with fewer confounding factors than in vivo methods. Accordingly, effects detected independently from the rest of the brain and macroscale network can lead to principles that apply throughout the broader neural circuitry.

In this report, we construct a novel, network-based model of the hippocampus, focusing on the DG, CA3, and CA1. We systematically validate the model activity by comparing simulations to existing measurements of activity rates of each neuron type, to reported frequency spectra from local field potential recordings, and to stimulus–response curves that qualitatively recapitulate input–output curves from in vitro recordings. Using this model, we examine the potential role of altered spike-timing-dependent plasticity on features of regional function, including activity rates, signal power, and interregional coupling. Although a modest plasticity deficit does not dramatically alter the overall pattern of activity, this injury mechanism does yield deficits in power across several frequency bands in CA3 and CA1. Given our results, we conclude that spike-timing-dependent plasticity (STDP) creates a delicate balance in the network and minor impairment can yield significant deficits in network function.

2 | METHODS

Given the body of work about the hippocampus, there are existing efforts to synthesize these data and construct computational models of its activity. However, these models predominantly consist of single, isolated subregions, making it impossible to interrogate aspects that depend on higher level circuitry or regional differences. (For the DG: Chavlis et al., 2017; Santhakumar et al., 2005; Strüber et al., 2017; Tejada et al., 2014. For CA3: Hummos & Nair, 2017; Sanjay et al., 2015; Stanley et al., 2013. For CA1: Cutsuridis et al., 2010; Fink et al., 2015; Malerba et al., 2016; Neymotin et al., 2011.) Impressive full-scale models of individual subregions exist (Bezaire et al., 2016; Dyhrfjeld-Johnsen et al., 2007), but these are slow and computationally expensive, often requiring supercomputers to run simulations. Such high computational requirements limit the accessibility and broad use of these models. Furthermore, the duration of the simulations is short (s), which precludes the study of adaptive mechanisms or prolonged change.

This reduced model represents the hippocampus as three interconnected subregions—the DG, CA3, and CA1—with topology based on the well-documented predominantly feedforward architecture of the hippocampus (Strange et al., 2014; Wheeler et al., 2015). It has 10 different types of neurons across the three subregions, and each neuron type is differentiated based on electrophysiological characteristics in the dynamic model and connectivity within and between

subtypes in the structural model. As a network model, each neuron is represented by a node, and the synaptic connections between neurons are edges. Our primary resources for the structure and connectivity of these regions were the Hippocampome database for overall information on neuron subtypes in the hippocampus (Wheeler et al., 2015), Morgan et al., 2007 and Dyhrfjeld-Johnsen et al., 2007 for the DG, and Bezaire & Soltesz, 2013 and Bezaire et al., 2016 for CA1.

2.1 | Structural model properties and circuitry

We narrowed our focus to three primary areas of the hippocampal formation with well-characterized structure and well-studied functions (Fanselow & Dong, 2010; Paterno et al., 2017; Wheeler et al., 2015). This subset of regions included the DG, CA3, and CA1. Within each subregion, we first determined which neuron types to include (Figure 1). Starting with all neurons identified in the Hippocampome database (83 different types across DG, CA3, and CA1) (Wheeler et al., 2015), we first eliminated any types without detailed electrophysiological characterization or connectivity information (see Section 2.2 for more information on the model of neural activity). We chose a point neuron model to reduce complexity and computation time (Izhikevich, 2003; Koch, 2004), as some neuronal types with unique morphologies yet similar electrophysiological characteristics could be combined in our model.

For each subregion (DG, CA3, CA1), point neurons were placed randomly on the surface of an ellipsoid. Each area is a separate ellipsoid, scaled by the anatomical dimensions of that subregion (Strange et al., 2014). The ellipsoid geometry has the advantages of mitigating edge effects and enhancing distance-dependent connectivity, such that neurons near one another are more likely to connect to one another. This approach is designed to mimic important aspects of the lamellar organization of the hippocampus in vivo (Andersen et al., 2000), while avoiding edge effects and more complex geometries. It approximates the physical aspects of the structure that are necessary for generating accurate network connectivity but does not create an exact physical representation of the hippocampus.

After finalizing the subtypes included in the model (Figure 1a,b), we determined the overall scale and number of neurons of each type. Once we identified the best possible estimates for the population

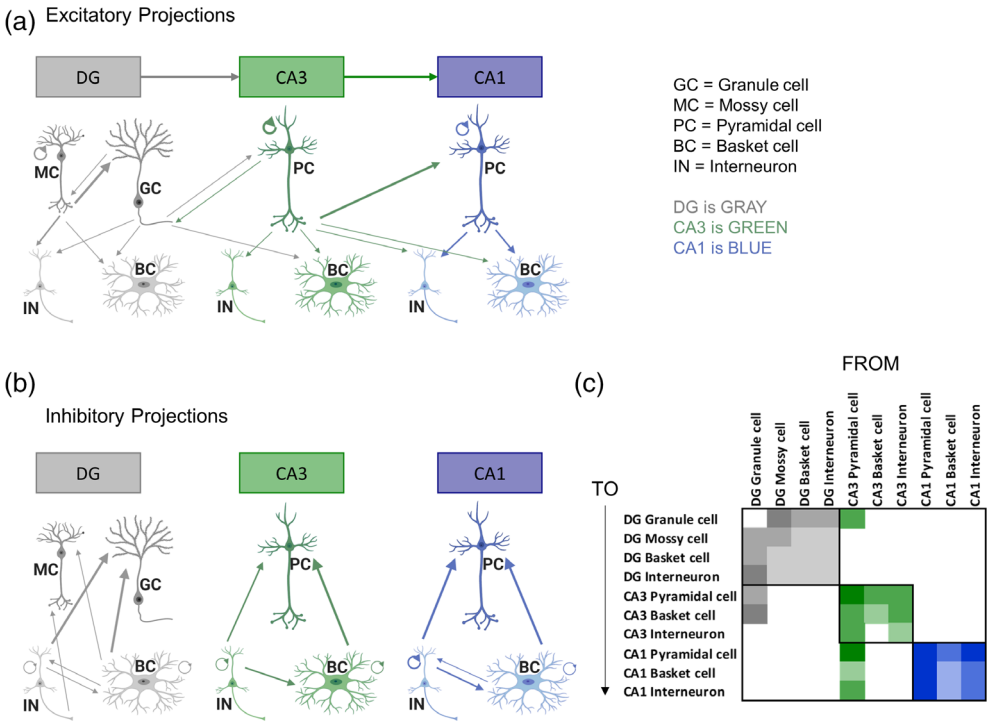

FIGURE 1 Model structure and circuitry. (a) The primary excitatory connections of the hippocampus follow a feedforward structure across three subregions (dentate gyrus [DG], CA3, CA1), as indicated by the top schematic. Each of 10 cell types is represented by an icon of a neuron with all excitatory connections between the 10 different cell types shown as arrows. Thick arrows represent many connections from a representative single neuron, and thin arrows represent few connections. The dentate is represented in gray, CA3 is green, and CA1 is blue. Thick arrows: $N > 40$. Medium arrows: $40 > N \geq 10$. Light squares: $N < 10$, where N is the average number of connections from a single upstream neuron to downstream neurons. Created with BioRender.com. (b) The inhibitory connections of the hippocampus are predominantly local, intraregional connections. Inhibitory connections between the 10 cell types are shown as arrows where arrow thickness corresponds to the number of connections. Created with BioRender.com. (c) This information is shown for both excitatory and inhibitory projections as a connectivity matrix. Moving down each column, a filled square indicates that connections exist. For example, DG granule cells project to DG mossy cells but not to other DG granule cells. Here, N is the total number of projections to a downstream subtype (number of connections per cell $\times$ number of cells). Dark squares: $N > 10{,}000$. Medium squares: $10{,}000 > N \geq 2000$. Light squares: $N < 2000$

numbers in vivo, we determined the ratio for each subtype relative to the primary excitatory subtype in each subregion (i.e., granule and pyramidal cells). For example, there are 56 pyramidal cells to 1 parvalbumin-expressing basket cell in CA1 (Bezaire & Soltesz, 2013). We used 10% total inhibitory neurons in CA1 and CA3 as an important constraint on population numbers, within the range of 10–12% reported empirically (Aika et al., 1994; Woodson et al., 1989) and similar to previous work (Bezaire et al., 2016; Bezaire & Soltesz, 2013). Given this constraint, we ensured that the sum of basket and generic interneurons comprised approximately 10% of the total number for CA1 and CA3. Importantly, we targeted an intermediate population scale for each cell type in the model, balancing the representation of different cell types with computational requirements. To ensure our model would run in a reasonable amount of time on a desktop computer, we limited the overall network size to under 10,000 neurons. The final network corresponds to a scale of approximately 1:200 for DG, 1:175 for CA3, and 1:150 for CA1, as compared to the rat hippocampus (see Table 1 for population sizes in the model).

To develop the connectivity matrix (Figure 1c), we found literature values for the number of connections between subtypes, relying primarily on Morgan et al. (2007) and Bezaire and Soltesz (2013). The connectivity rules were developed via the following formula:

$$C_{\text{model}} = \frac{C_0}{N_0} \times k(N_{\text{model}})$$

where C_{model} is the number of connections per neuron in the model, C_0 is the original number of connections between two subtypes in vivo, N_0 is the original population size in vivo, N_{model} is the population size of the subtype in the model, and k is a scalar. Given the reduced population sizes, we increased the density by a constant scalar (k) for each area to generate synaptically driven activity. This method is similar to that used in other models that are not full-scale (Morgan et al., 2007; Santhakumar et al., 2005; Tejada et al., 2014) (see Table 2 for connectivity values between all subtypes). Given that

TABLE 1 Cell numbers and percentages for different cell types. This is the final set of cell types included in the hippocampal model

Cell type	Number	Percentage
DG granule	5000	56.3
DG mossy	150	1.7
DG basket	50	0.6
DG interneuron	60	0.7
CA3 pyramidal	1250	14
CA3 basket	30	0.3
CA3 interneuron	120	1.4
CA1 pyramidal	2000	22.5
CA1 basket	45	0.5
CA1 interneuron	180	2
Total	8885	100

Abbreviation: DG, dentate gyrus.

TABLE 2 Average number of connections from a cell of one subtype to another. It is formatted as N connections from column subtypes to row subtypes. (e.g., each DG basket cell has an average of 63 connections to DG granule cells)

	DG granule cell	DG mossy cell	DG basket cell	DG interneuron	CA3 pyramidal cell	CA3 basket cell	CA3 interneuron	CA1 pyramidal cell	CA1 basket cell	CA1 interneuron
DG granule cell	0	1625	63	160	7	0	0	0	0	0
DG mossy cell	1	18	4	4	0	0	0	0	0	0
DG basket cell	1	1	2	1	0	0	0	0	0	0
DG interneuron	3	12	1	3	0	0	0	0	0	0
CA3 pyramidal cell	2	0	0	0	45	100	20	0	0	0
CA3 basket cell	5	0	0	0	5	3	20	0	0	0
CA3 interneuron	0	0	0	0	2	0	2	0	0	0
CA1 pyramidal cell	0	0	0	0	75	0	0	20	90	130
CA1 basket cell	0	0	0	0	1	0	0	10	8	15
CA1 interneuron	0	0	0	0	2	0	0	15	6	20

Abbreviation: DG, dentate gyrus.

this model relies on point neurons rather than multicompartmental neurons, the synapses between cells are represented as aggregate connections. For the interregional connectivity, we relied on similar calculations to determine the number of connections, but in contrast to distance-dependent intraregional connections, connections between subregions were added to randomly selected neurons. Although most collaterals from CA3 feedforward to CA1, CA3 is known to have some recurrent collaterals and a small backprojection to the DG. In our model, 60% of collaterals project to CA1, 35% of collaterals are recurrent, and the remaining 5% comprise the backprojection to DG (Myers & Scharfman, 2011; Treves & Rolls, 1994; Wittner et al., 2007).

2.2 | Dynamic model features

Action potential spiking was modeled with the Izhikevich system of differential equations, applying the 2008 formulation as follows (Izhikevich & Edelman, 2008):

$$Cv' = k(v - v_r)(v - v_t) - u + I$$

$$u' = a[b(v - v_r) - u]$$

$$\text{if } v \geq v_p, \text{then} \begin{cases} v = c \\ u = u + d \end{cases}$$

where v is the membrane potential in millivolts (mv), and u is the recovery variable. C is the membrane capacitance (pF), v_r is the resting membrane potential, v_t is the threshold potential, and v_p is the membrane potential at the peak of the spike. I is the current in picoamperes (pA). The dimensionless parameters a, b, c, d, and k are used to tune the spiking behavior of each neuron subtype (see Izhikevich & Edelman, 2008 and Izhikevich, 2010 for more detail). The current (I) can be decomposed according to the following equation:

$$I = I_{\text{AMPA}} + I_{\text{NMDA}} + I_{\text{GABA}} + I_{\text{noise}}$$

The total current aggregates ionic currents through AMPA, NMDA, and GABA-A receptors as well as a noise input used to drive the network, using a gamma distribution ($k = 2$, $\theta = ½$) (Gabrieli et al., 2020; Gabrieli et al., 2021; Izhikevich & Edelman, 2008; Schumm et al., 2020) (see Section 2.3 for more detail on the noise current). The NMDA receptor currents have longer duration and shorter amplitude as compared to AMPA receptor currents (Gabrieli et al., 2021). Electrophysiology data were compiled for all relevant subtypes from the Hippocampome and NeuroElectro databases, whenever available (Tripathy et al., 2014; Wheeler et al., 2015). Where possible, we implemented values for resting membrane potential (v_r), threshold potential (v_t), and capacitance (C) directly into the model equations above. We used the average values and tuned the parameter up or down within the experimentally recorded range to match the firing pattern of each cell type. If the capacitance for a subtype was unknown, we used 115 pF, the average recorded across all neuron subtypes documented in the NeuroElectro database (Tripathy et al., 2014). Values for the membrane time constant, action potential width, and afterhyperpolarization were similarly included, with more qualitative adjustments (see Tables A1—A3 in the Appendix for electrophysiological properties of relevant neuron types). The remaining parameters were modified to match examples of cell firing patterns found in the literature. A good match was determined based on firing rate and action potential shape across a range of current injections, which included a subthreshold injection, a marginally supra-threshold injection, and one to two larger injections, depending on the available data.

After developing neuron models for all subtypes under consideration, we merged the models for neuron types with similar electrophysiology, producing 10 final neuron models. (See Table 3 for the full set of parameters used. Single cell activity traces for each subtype can be found in Table S1 in Supporting Information and display predominantly regular spiking patterns. Table S2 contains more detailed experimental electrophysiology references that were used in model development and all of which are drawn from the Hippocampome and NeuroElectro databases.) To introduce heterogeneity among neurons within a specific type, we varied model parameters ±10–20% of the nominal values. None of these adjustments to model parameters

TABLE 3 Neuron model parameters

Cell type	V_r	V_t	V_p	C	a	b	c	d	k
DG granule	−70	−48	30	60	0.01	1.2	−68	25	0.7
DG mossy	−62	−37	30	50	0.01	3	−65	50	1
DG basket	−62	−38	35	150	0.01	6	−75	25	1
DG interneuron	−65	−43	30	90	0.25	2.5	−70	30	1
CA3 pyramidal	−68	−50	30	200	0.01	3	−70	50	1
CA3 basket	−57	−34	25	150	0.25	5	−70	50	1
CA3 interneuron	−60	−40	30	140	0.4	4	−70	40	1
CA1 pyramidal	−65	−50	35	125	0.2	10	−68	100	2
CA1 basket	−60	−40	30	140	0.02	0.9	−65	15	1
CA1 interneuron	−60	−38	30	130	0.15	2.25	−68	40	1

Note: V_r = resting membrane potential; V_t = instantaneous threshold potential; V_p = spike peak membrane potential; C = capacitance; a, b, c, d, and k are dimensionless model parameters.

altered the characteristic firing patterns of these neurons. The ranges of interneuron parameters were slightly broader than the other neuron types (±20 vs. ±10%) to represent the diversity of interneurons. This variability is more representative of heterogeneous in vivo neuron populations, in which no two neurons are the same (Izhikevich, 2003). Small variations in parameters also prevent instability in model dynamics, which can occur when all simulated neurons are identical.

We implemented propagation delays based on the physical distances between neurons where the minimum delay is 1 ms. The ranges used were based on an average 0.2 m/s conduction velocity (Kress et al., 2008; Meeks & Mennerick, 2007; Miles et al., 1988) and the lower range of delays reported for Schaffer collaterals (Andersen et al., 2000). Within-region delays range from 1 to 6 ms, and between-region delays are estimated to be 6–10 ms. To account for slower conduction velocity in the DG compared to CA3 (Kress et al., 2008), we used a different range of delays for each subregion (see Table 4). At this scale, the difference is only 1–2 ms at the maximum delay.

Finally, the excitatory–excitatory AMPA synaptic connections in the network are plastic, governed by both STDP and homeostatic plasticity (HSP). STDP is a classical implementation of order-dependent Hebbian learning by which the synaptic strength between two neurons is strengthened if they fire causally. If neurons do not fire causally (the downstream neuron fires prior to the upstream neuron), the synaptic strength is instead decreased, according to the following equation (Effenberger et al., 2015):

$$\Delta w(w) = \begin{cases} A_+(w)\exp\left(-\dfrac{t_{\text{post}} - t_{\text{pre}}}{\tau}\right) \text{ if } t_{\text{post}} - t_{\text{pre}} > 0 \\ A_-(w)\exp\left(-\dfrac{t_{\text{post}} - t_{\text{pre}}}{\tau}\right) \text{ if } t_{\text{post}} - t_{\text{pre}} \le 0 \end{cases}$$

where w is the weight of the connection between two neurons. A_+ and A_- determine the magnitude of maximal synaptic change. The A_+/A_- ratio is commonly biased slightly toward strengthening and was set to 1.05. τ is the plasticity time constant and often approximated as 20 ms. Finally, t_{pre} and t_{post} are the timing of presynaptic and postsynaptic spikes, respectively. Neurons were also desensitized to rapidly repeated inputs at 40% attenuation ($\tau_{\text{desensitization}} = 150$ ms) (Izhikevich & Edelman, 2008).

TABLE 4 Propagation delays between neurons. Delays are reported in ms and are implemented as integers only. Within subregions, delays follow a distance-dependent distribution based on the physical distance between neurons. Between different subregions, they follow a uniform distribution

Delay type	Range (ms)	Distribution
Within DG	1–6	Distance dependent
DG → CA3	6–10	Uniform
CA3 → DG	6–10	Uniform
Within CA3	1–4	Distance dependent
CA3 → CA1	6–10	Uniform
Within CA1	1–6	Distance dependent

Abbreviation: DG, dentate gyrus.

As in many previous models, we applied STDP to AMPA synapses between excitatory neurons only because inhibitory STDP is not well understood and warrants ongoing investigation (Caporale & Dan, 2008; Lu et al., 2007). However, it is a well-known problem that STDP alone can produce chronic runaway firing rates in such models, potentiating or depressing synapses endlessly (Zenke et al., 2017). Therefore, to combat drifting activity, we incorporated HSP to stabilize synapses (Turrigiano et al., 1998; Turrigiano & Nelson, 2004). Among the many proposed mechanisms for synaptic stabilization (inhibitory synaptic plasticity, neuromodulation, synaptic normalization, etc.), we chose synaptic scaling for two key reasons. It is comparatively well-characterized and enables us to continue to test STDP-dependent learning. The specific implementation we used was gated, weight-dependent synaptic scaling. Synaptic scaling is a heterosynaptic form of plasticity because it modifies all synapses of a neuron, rather than acting on the level of individual synapses. By comparing the actual neuron firing rate to a target firing rate, this homeostatic mechanism decreases synaptic weights if activity is too high and increases them if it is too low. Adapted from Effenberger et al. (2015), the following equation demonstrates this property:

$$\text{if } |(v_o - v_t)/v_t| > 0.50$$

$$\Delta w(w) = -\frac{\gamma}{W_{\max}}\left(\frac{v_o - v_t}{v_t}\right)(w^2)$$

where w is the weight of connection, γ is the dimensionless rate of change and equals 10^{-8} in our simulations, v_o is the observed firing rate, v_t is the target firing rate, and $W_{\max}$ is the maximum excitatory weight for that neuron type. Since STDP acts only on excitatory-to-excitatory connections, synaptic scaling also applies to these connections. Previous studies have demonstrated the importance of weight dependence for synaptic stabilization (Effenberger et al., 2015; Tetzlaff et al., 2011). Finally, to preserve diversity and competition among synapses, HSP applies in neurons with firing rate change greater than 50% of their target firing rate (v_t) over the course of 120 s. This threshold is important because it avoids over-constraining the model and continues to allow neurons to adapt with STDP. Given we intend to study STDP-dependent learning in future work with this model, this is an important aspect to our solution to synaptic weight stabilization.

As the slow rate of HSP can significantly decrease the speed of network convergence (Effenberger et al., 2015), we first settled the network for 20 min with STDP only to accelerate convergence. We used the individual neuron firing rates during minute 20 to set the target firing rates for each neuron. We then turned on HSP and ran the simulation for an additional 30 min with a fixed timestep of 0.2 ms. All data analyzed were taken from the final 5 min of simulation, after the network has stabilized with both STDP and HSP. See Figure S1 in Supporting Information.

2.3 | Connection strength and noise calibration

Incorporating unique electrophysiology-based parameters for each neuron subtype required calibrating the connection strength and noise stimulus for each subtype. The noise stimulus is designed to cause each neuron to spike once per second at a random timestep. Since the firing is noisy and uncoordinated, the noise input lacks the spectral features of a 1 Hz signal. To maintain 1 Hz noisy firing across the entire network, each subtype needed a different stimulus magnitude. Otherwise, with each noise input, some neurons would spike multiple times and others not at all. For calibration, we used a single neuron model and first verified that the neuron did not spike with a current injection of 0 pA. Then we increased or decreased the current and observed the size of the excitatory postsynaptic potential (EPSP) or the inhibitory postsynaptic potential (IPSP), respectively. The current stimulus was instantaneous and allowed to decay. The excitatory strength was set such that an injection of that size produced an EPSP size less than 10 mV (Ferster & Jagadeesh, 1992) and it would take approximately three coincident inputs to produce an action potential. Accordingly, the noise value for each neuron was set to 2-3x the excitatory strength so that the neuron would spike only once from resting membrane potential. Similar to excitatory strength, the inhibitory strength was determined by identifying the current required for an IPSP size of approximately 15 mV (Ferster & Jagadeesh, 1992). This calibration process ensured consistency among subtypes and agreement with the literature (Ferster & Jagadeesh, 1992).

2.4 | Analysis metrics

All metrics were computed for the final 5 min of simulation time. To evaluate average firing rate, we summed the number of spikes for each neuron for the last 5 min of simulation activity and divided by the duration for an average in Hz. Values reported for an entire subtype are the mean of firing rates for that subtype. The variability in spike timing was quantified as the coefficient of variation of the interspike interval (CoV ISI), which is the *SD* over the mean of the interval between spike times. The metric contextualizes firing rate by measuring the irregularity of spike timing such that larger values indicate greater variability in duration between spikes. The CoV ISI was computed for each neuron and averaged by subpopulation. To measure prominent frequencies in network activity, all spikes were summed for each millisecond for each region (DG, CA3, CA1). For each trace, the signal was smoothed and analyzed in the frequency spectrum by Welch's method. The power was computed in five different frequency bands, corresponding to delta (<3 Hz), theta (3–8 Hz), alpha (8–12 Hz), beta (13–25 Hz), and gamma waves (25–60 Hz) (Abhang et al., 2016; Bezaire et al., 2016; Rutishauser et al., 2010).

Since we were interested in the relationship between traces extracted from these frequency bands, we assessed phase coherence between the theta signal component in CA3 and CA1. We applied a Hilbert transform to the theta wave to calculate the analytic signal from which we extracted the phase angle. With the phase components of both CA3 and CA1 signals, we computed the phase locking value (PLV) according to the following equation:

$$\mathrm{PLV} = \left| \frac{\sum_{t=1}^{n} e^{i(\theta_1 - \theta_2)}}{n} \right|$$

where n is the length of the trace, t is a timestep, θ_1 is the phase angle of trace 1, and θ_2 is the phase angle of trace 2. Finally, we evaluated phase-amplitude coupling (PAC) between the theta wave and gamma oscillation in CA1. Similar to the coherence analysis, we filtered the aggregate activity, applied a Hilbert transform, and extracted the phase and amplitude components from the theta and gamma bands, respectively. The phase angle is then binned into 18 bins of 20° (Tort et al., 2008), and the corresponding amplitudes are averaged for each phase bin, yielding a phase-amplitude plot. PAC exists when this distribution differs significantly from the uniform distribution. To measure this difference, we calculated the modulation index (MI) as follows:

$$\mathrm{MI} = \frac{\log(N) + \sum_{j=1}^{N} a(j) \log[a(j)]}{\log(N)}$$

where N is the number of phase bins (18 in this study) and a is the vector of normalized average amplitudes per phase bin. To determine significance for both coherence and cross-frequency coupling, we compared the experimental values to values generated from null models. Following a method promoted by Hülsemann et al., we generated permuted activity traces by randomly cutting the trace in two parts, flipping both parts, and concatenating (Hülsemann et al., 2019). The procedure alters the precise timing of the signal but leaves the frequency information intact, so it is an effective and conservative method of permutation testing (Hülsemann et al., 2019). Permutation testing was repeated 100 times for each network, and those values were averaged to yield one null model value for each network.

2.5 | Stimulus–response curve and stimulation

To demonstrate an input–output relationship in this circuitry, we developed a protocol which is analogous to classical input–output curves in acute slice electrophysiology: (1) stimulate the DG and record in the DG and (2) stimulate CA3 and record in both CA3 and CA1. These protocols are designed to mimic perforant path and Schaffer collateral stimulation, respectively. For each, we selected nonoverlapping groups of stimulated and recording neurons. The stimulated subset consisted of randomly selected neurons, which simultaneously received an input equivalent to five spikes. The response was measured from the set of recording neurons, which consisted of the neurons nearest a randomly chosen location in the network. The recording set sizes are 100 neurons in DG and 50 neurons in CA1, which are 2 and 4% of the populations in the DG and CA1, respectively.

The stimulus consists of linearly increasing the number of stimulated neurons by targeting 10% more with each stimulus level. If we

consider an example of stimulating area CA3, stimulus level 1 targets five neurons, which is 10% of the overall stimulation subset in CA3. Stimulus level 2 targets 10 neurons, which is 20% of the total stimulated neurons, and so on for increasing levels of stimulus up to level 10. This simulates linearly increasing input current in electrophysiology protocols. The size of the recording group remains constant, and the response is the sum of all spikes from the subset of neurons normalized by the maximum response for that network. The 1 Hz noise used to drive the network in other simulations was removed during this procedure to enhance the signal-to-noise ratio. This protocol was run for each of the 10 baseline networks.

2.6 | Injury: Impaired STDP

To simulate plasticity impairment in the model, we reduced the maximum potentiation constant (A_+ in the STDP equation above) by 10%. After this change, the networks resettled their AMPA-based synaptic weights for 30 min with intact HSP and impaired STDP mechanisms, and the analysis focused on the last 5 min of this simulation time. By this time, the activity level had stabilized at a level distinct from baseline. While there are several possible ways to alter the STDP algorithm, we believe this modification most closely represents empirically observed changes, such as the inability to induce LTP in CA1 after injury. Others have demonstrated that this ability is associated with protein production, receptor replacement and lifetime, and CaMKII phosphorylation (Schwarzbach et al., 2006; Vogel et al., 2017). Inhibition of these processes would reduce the overall capacity for potentiation. In our model, this impediment is captured by reducing the maximum amount of positive synaptic change associated with STDP. The precise decrement was determined by identifying a change after which the network could stabilize after 30 min. At higher levels of injury (>10% decrease), activity continued to decline, and the network did not achieve a new equilibrium level of activity.

2.7 | Statistical analysis

To compare coherence and cross-frequency coupling between baseline simulations and null models, we used Student's *t* test. To compare models with STDP impairment with their respective baseline measures, we applied a paired Student's *t* test. Bonferroni corrections were used to determine significance when there were pre- to post-injury comparisons for many groups, such as different neuron subtypes.

3 | RESULTS

3.1 | Firing rate and frequencies of activity

With representative modeling parameters to describe four excitatory and six inhibitory neuron populations across three anatomic subregions,

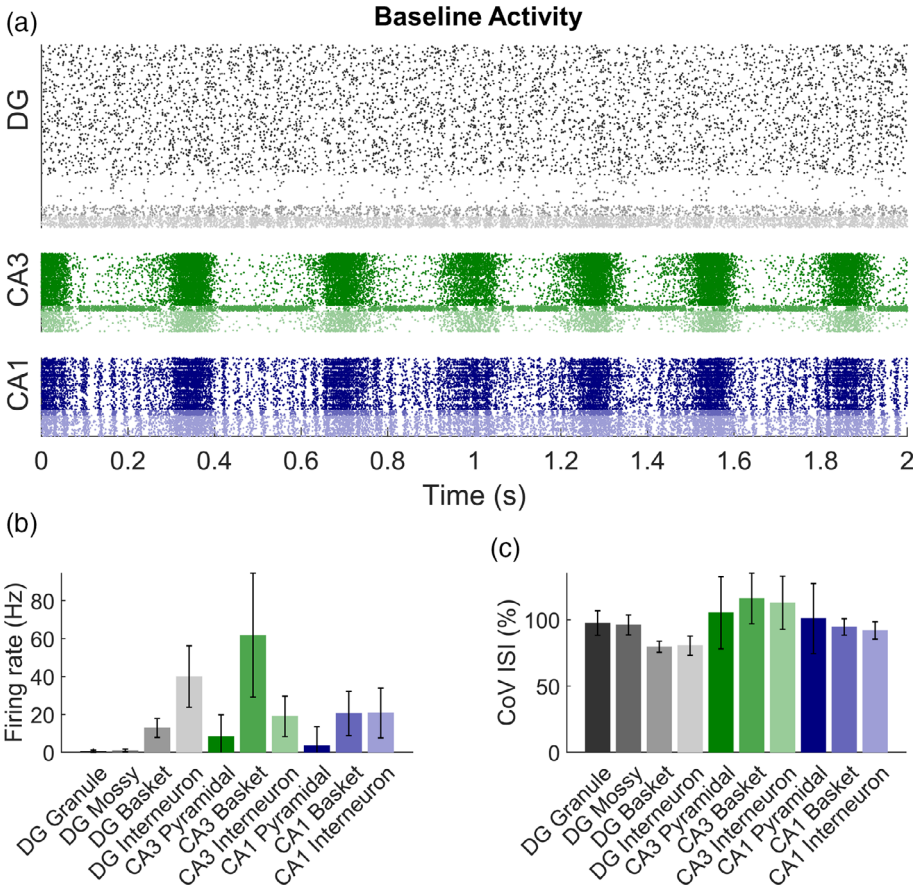

FIGURE 2 Baseline activity results establish functional network behavior. (a) The raster plot displays the baseline activity where each dot represents a spike. The primary excitatory cell types (dentate gyrus [DG] granule cells, CA3, and CA1 pyramidal cells) are shown in the darkest colors. Inhibitory neurons are shown in lighter colors, which match those in panels (b) and (c). DG = gray; CA3 = green; CA1 = blue. (b) Average firing rates by cell type, evaluated over 5 min of simulated time. Inhibitory populations have higher firing rates than excitatory populations do, on average. (c) Average coefficient of variation of the interspike interval (CoV ISI) by cell type. CoV ISI was evaluated over 5 min of simulated time and varies less by cell type than firing rate does

our model showed distinct patterns of activity in each anatomic area (Figure 2a). Broadly, neural activity was lowest in the DG and higher in both CA3 and CA1 (Figure 2). The average firing rates of the neuron subtypes also reflected these differences (Figure 2b). As expected, the excitatory neurons had lower firing rates than the inhibitory neurons (excitatory: 2.4 ± 7.2 Hz vs. inhibitory: 24.4 ± 18.7 Hz; Student's *t* test; $p < .001$). Across all subtypes, the average firing rates fell within the range reported for the literature (see Table A4 in the Appendix). Whenever the data were available, we used the spontaneous firing rate for the lower limit and the maximum recorded firing rate for the upper limit for comparison purposes. We also compared to existing models where possible. Compared to firing rate, the CoV ISI was more consistent across subtypes; however, as one might expect, there were still differences across the subregions (DG: 97 ± 10% vs. CA3: 106 ± 27% vs. CA1: 100 ± 25%; one-way analysis of variance; $p < .001$) (Figure 2c). To further contextualize these firing rate results, we also assessed network sparsity by calculating edge density according to the following equation:

$$D = \frac{K}{N^2 - N}$$

where D is the density, K is the number of connections or edges, and N is the number of neurons in the network. The overall networks are sparse, with a density of 0.008. The subregional densities for the DG, CA3, and CA1 are 0.010, 0.038, and 0.024, respectively. Therefore, we see that the region with the highest density, CA3, also has the highest firing rate.

Once we established agreement between the simulation results and the available literature, we next considered the general spectral features of activity within each anatomic area. Attributes of the frequency spectrum are important for regional function and communication between regions (Battaglia et al., 2011; Colgin, 2016), and the spectra provide a framework to investigate how changes to the network (e.g., trauma) would affect the flow of information through the circuit. We summed the activity of each subregion into an aggregate signal, which we smoothed with a 10 ms moving average filter and evaluated in the frequency spectrum (Figure 3a). We calculated the power in several frequency bands that are often used to classify electrode recordings in the brain (delta: <3 Hz, theta: 3–8 Hz, alpha: 8–12 Hz, beta 13–25 Hz, and gamma: 25–60 Hz). In this baseline state, the DG did not have high power in any of these bands (Figure 3b), indicating that the area does not generate prominent frequencies of its own (mean power < 0.06 across all frequency bands). Rather, the DG operates as a gate, or filter, for the rest of the hippocampal circuitry, only allowing important signals to pass through to downstream regions. In vivo the DG exhibits more dynamic spectral activity as a result of extra-hippocampal stimulation in the behaving animal. CA3 was dominated by low frequency signals in the delta and theta frequencies (mean power > 2.4) (Figure 3c). CA3 shows little to no

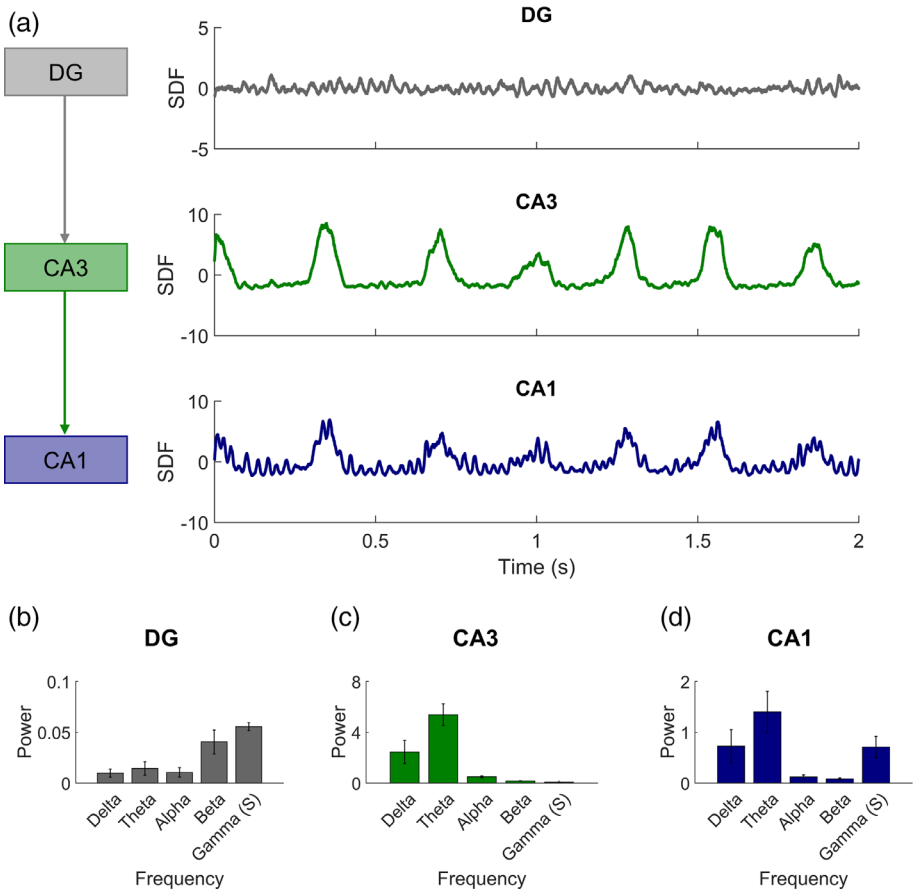

FIGURE 3 The observed power in common frequency bands supports known characteristics of each subregion. (a) Aggregate activity signals for each area are computed by summing the spiking activity at each ms and smoothing the resulting signal with an average filter to yield the spike density function (SDF). These traces were evaluated in the frequency spectrum to test power in each of five common frequency bands of brain activity. (b) Compared to CA3 and CA1, the dentate gyrus (DG) has low power in all frequency bands, but the frequencies with the most power are beta and slow gamma. (c) CA3 has signal in relatively low frequencies of the delta and theta bands. (d) CA1 has power in both theta and slow gamma bands

power in alpha, beta, or gamma frequencies (mean power < 0.5). The development of these low frequency signals in CA3 despite minimal passthrough from the DG points to the importance of recurrent collaterals in CA3 (see Figure S2 in Supporting Information for additional evidence to this effect). Supporting the putative function of CA3 as an amplifier, recurrent connections enable the subregion to augment signals and send them to CA1. Uniquely, CA1 demonstrates power in both low frequency theta and higher frequency gamma (Figure 3d). These frequencies are believed to enable communication between CA1 and other brain regions, such as the entorhinal cortex, CA3, and prefrontal cortex (Colgin et al., 2009; Tamura et al., 2017), by directing the transient binding between distant neuronal ensembles (Colgin et al., 2009). In the complete biological circuit, these frequencies would be sent from CA1 to downstream regions, fulfilling the primary function of CA1 as a transducer (Cohen et al., 2007). Importantly, all these frequencies developed organically within the network based on the neuron model parameters and connectivity. It is driven by synaptic noise to generate nominal random firing, but there are no additional patterns or frequencies used as inputs. Altogether, these results validate the activity of the model and demonstrate that the circuitry supports known functions of each subregion.

3.2 | Baseline networks produce stimulus–response curves

We next sought to demonstrate an important feature of hippocampal circuitry—namely, the relationship between extrinsic stimulus and the circuit response. In electrophysiology, extracellular field recordings are used to evaluate field potential input–output relationships and to test the function and excitability of a hippocampal slice. The method typically consists of stimulating with a current input and recording the downstream circuit response. The two most common protocols in the hippocampus are stimulating the perforant path and recording in downstream DG (Figure 4a) or stimulating the Schaefer collaterals in CA3 and recording in downstream CA1 (Figure 4c). We developed an analogous testing routine within our model (see Section 2 for details). Briefly, with each increase in stimulation level, more neurons fired action potentials. The response in terms of spikes was recorded from a nonoverlapping set of neurons and normalized. The resulting curves show that as the stimulation level increases, there is a corresponding increase in the response (number of spikes). As stimulation continues to increase, the response reaches a plateau, producing a curve. We see that this is the case for both perforant path- and Schaeffer collateral-like stimulation (Figure 4b,d). We also fit the curves with two-term exponential equations ($Y_{fit} = a \times \exp(b \times x) + c \times \exp(d \times x)$. DG: $a = 0.40$, $b = 0.076$, $c = -0.40$, $d = -1.54$; $R^2 = .98$; RMSE = 0.04. CA3: $a = 1.50$, $b = -0.04$, $c = -1.50$, $d = -0.21$; $R^2 = .98$; RMSE = 0.04. CA1: $a = 0.73$, $b = -5.6e\text{-}6$, $c = -0.72$, $d = -0.45$; $R^2 = .95$; RMSE = 0.05.) Although this approach differs from classical electrophysiology because the stimulus consists of spikes as an analog to extracellular current injection, we find a similar stimulus–response trend.

3.3 | Phase coherence and PAC

To further explore the relationships between frequency bands of the aggregate activity traces, we considered phase coherence between the phase angles of the CA3 and CA1 theta waves. We filtered the

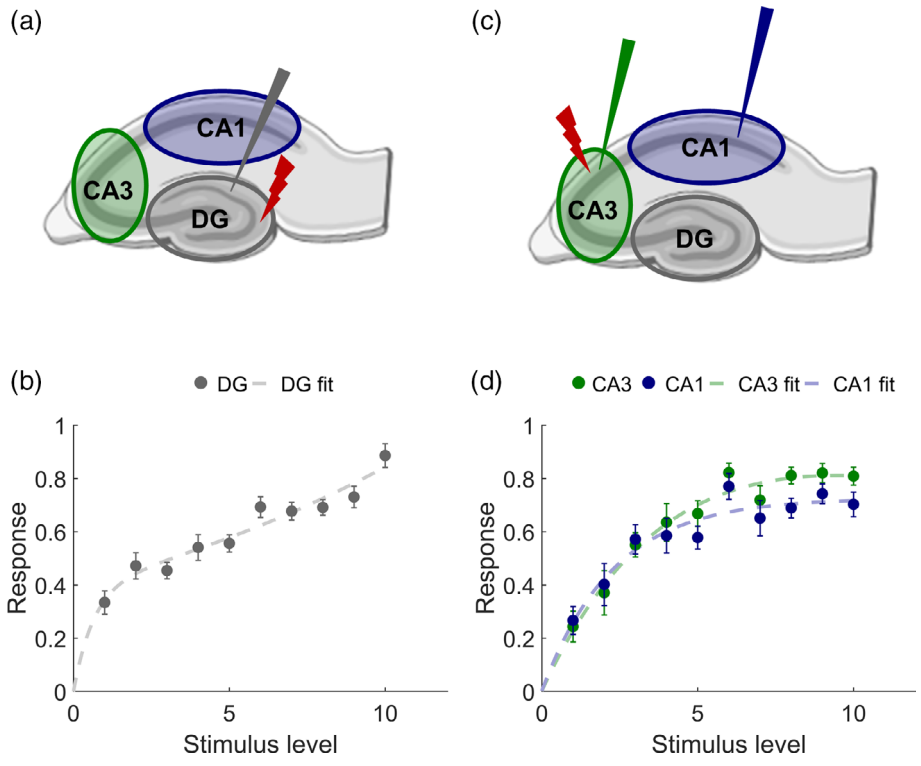

FIGURE 4 Stimulus–response curves in the model hippocampus. (a) The schematic shows how traditional input–output curves would be recorded in acute slices. The red bolt is a hypothetical stimulus, and the gray triangle represents a recording electrode in the dentate gyrus (DG). (b) In the model DG, the response has higher variability at low stimulus levels and is more stable at higher levels. Error bars = *SEM*. (c) This schematic shows stimulus (red bolt) of the Schaffer collaterals, which project from CA3 and synapse in CA1. The green triangle represents a recording electrode in CA3 while the blue triangle signifies a recording electrode in CA1. (d) In the model, the normalized response tracks closely between CA3 and CA1. Error bars = *SEM*

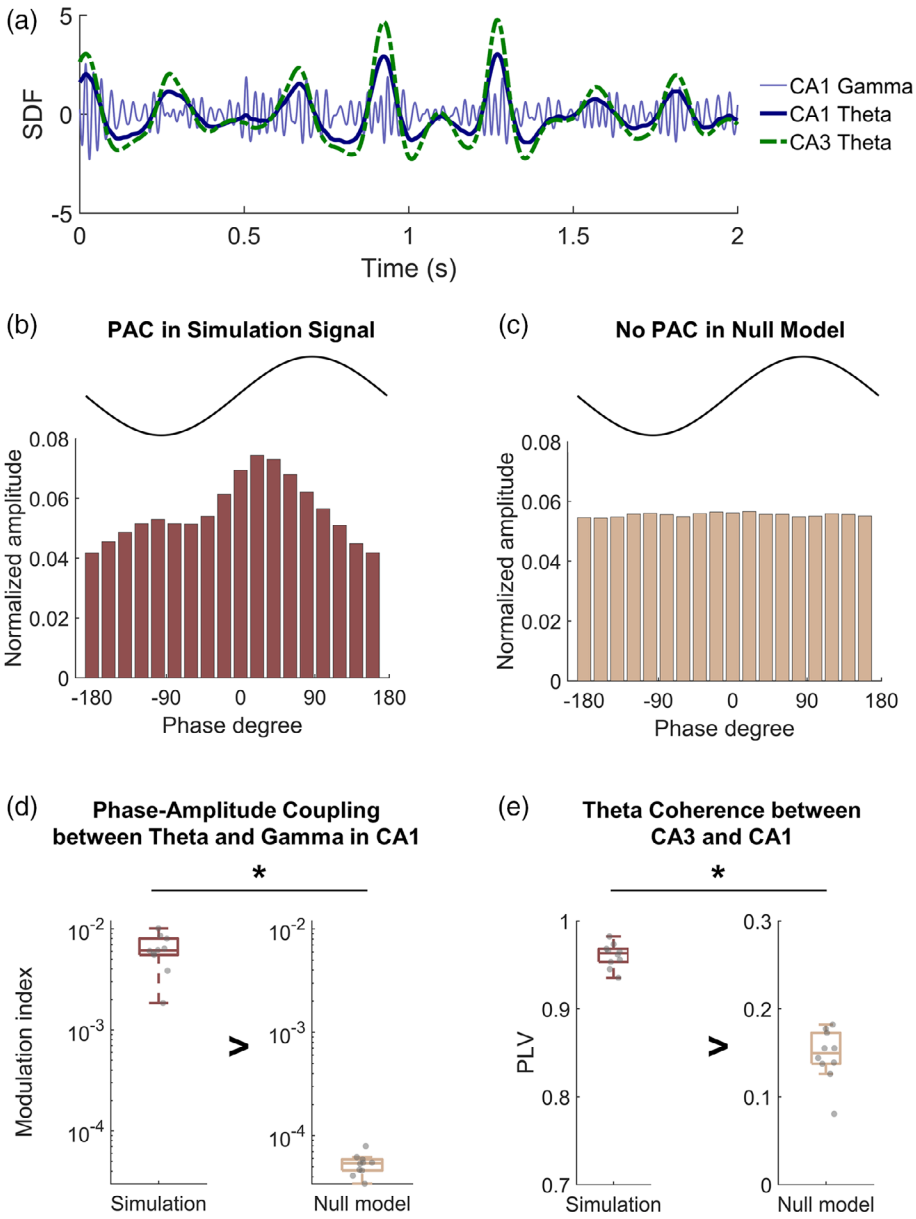

FIGURE 5 There is strong phase-amplitude coupling (PAC) in CA1 and phase coherence between CA3 and CA1 at baseline. (a) The aggregate activity from CA3 and CA1 was smoothed and filtered by frequency band. (b) A phase-amplitude plot demonstrates the presence of phase-amplitude coupling between the theta and gamma frequencies in the CA1 subregion. The amplitude of the gamma wave is highest during the rising phase of the theta wave. (c) The null model generated by permuting the gamma trace produces a uniform phase-amplitude distribution, indicating no phase-amplitude coupling. (d) The modulation index is much higher for the simulation signal than for the null model (p < 1e-5). (e) The phase locking value (PLV) between the theta wave in CA3 and CA1 is high, suggesting a high level of phase coherence (p < 1e-5)

traces (Figure 5a), extracted the phase component from the analytic signal, and computed the PLV according to the method originally introduced by Lachaux et al. (1999). Across the 10 networks, the coherence between CA3 and CA1 theta oscillations is high and significant compared to null models (simulation: 0.96 ± 0.01 vs. null model: 0.15 ± 0.03; p < 1e-5) (Figure 5e). This suggests that theta oscillations are highly synchronized between CA3 and CA1, which can also be seen in the filtered traces (Figure 5a). We also evaluated cross-frequency coupling between theta and slow gamma frequencies in CA1. Specifically, we tested for PAC where the phase of the theta wave corresponds to the amplitude of the gamma wave. Qualitatively, the representative phase-amplitude plot shows that there is a strong relationship between the theta phase and gamma amplitude (Figure 5b). The same plot for permuted data yields a uniform distribution, indicating there is no cross-frequency coupling (Figure 5c). Quantitatively, permutation testing demonstrates that the MI is significantly higher in the simulation data than in the null model (simulation: 6.2e-3 ± 2.3e-3 vs. null model: 5.3e-5 ± 1.2e-5; p < .001) (Figure 5d). It is important to note that the peak of the gamma amplitude is located at the rising phase of the idealized theta wave (Figure 5b). This result differs from other work that shows the amplitude peak near the trough of the theta wave (Bezaire et al., 2016; Tort et al., 2008). It is possible this difference arises because our analysis aggregates the simultaneous spiking activity across the entire simulated subregion, and in this way, it is not a true local field potential (LFP). Furthermore, in vivo recording data demonstrate that the theta phase preference of the gamma amplitude varies based on attributes like the behavioral state of the animal and the specific gamma sub-band of interest (Belluscio et al., 2012).

3.4 | STDP impairment

After STDP impairment, we find that the overall pattern of activity remains similar to baseline (Figure 6a). Several neuron subtypes do

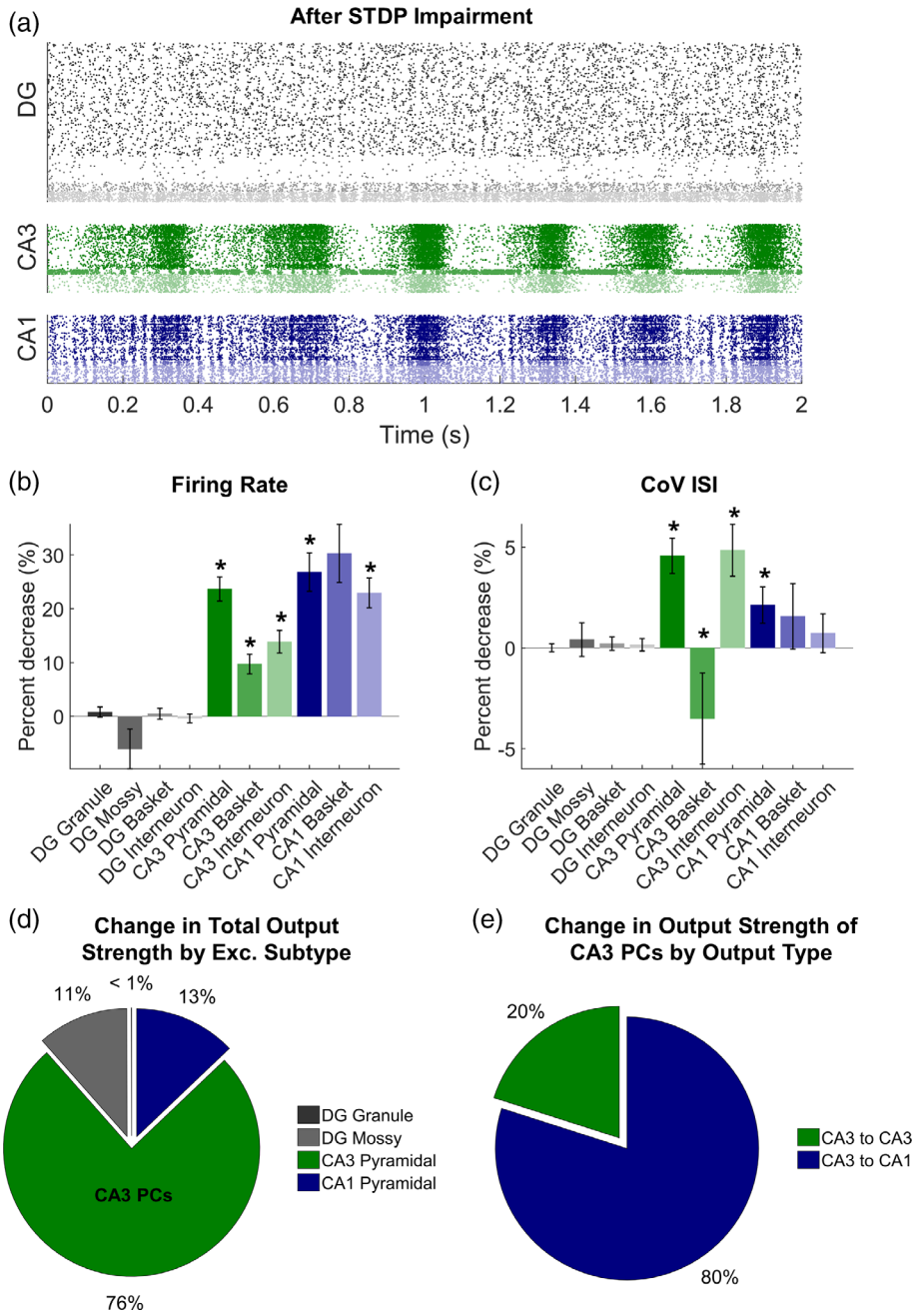

FIGURE 6 Impaired spike-timing-dependent plasticity (STDP) decreases activity in CA3 and CA1. (a) A raster plot of activity after injury shows a similar pattern to baseline activity. (b) CA1 has the largest percentage decrease in firing rate. Asterisks (*) indicate significant difference between firing rate at baseline versus injury (paired *t* test with Bonferroni correction; $p < .005$). (c) The coefficient of variation of the interspike interval (CoV ISI) alters the most in the CA3 subregion. Asterisks (*) mark significant differences between CoV ISI at baseline versus injury (paired *t* test with Bonferroni correction; $p < .005$). (d) CA3 pyramidal cells (PCs) account for the largest percentage change in the total output strength of the network. (e) Most of the change in output strength of CA3 PCs is in their synapses onto CA1 pyramidal cells

however have a significant reduction in their firing rates compared to baseline levels (CA3 pyramidal cells, CA3 basket cells, CA3 interneurons, CA1 pyramidal cells, CA1 interneurons; paired Student's *t* test for each cell type; $p < .005$ with the significance level determined by Bonferroni correction for multiple comparisons) (Figure 6b). Several subtypes also have significant changes in the CoV ISI. A decrease in the CoV ISI indicates less variability in the timing of neuron firing and was observed for CA3 pyramidal cells, CA3 interneurons, and CA1 pyramidal cells (Figure 6c). Uniquely, CA3 basket cells exhibited a significant increase in CoV ISI (paired Student's *t* test; $p < .01$ for all baseline to injury comparisons) (Figure 6c). None of the dentate subtypes had significant alterations in their activity. These activity changes were related to changes in synaptic strength. Of the overall change in weight, CA3 pyramidal cells accounted for the majority at 76% (Figure 6d). When we divided this change among the outputs of the CA3 pyramidal cells, we found that 80% of the change was in synapses onto CA1 pyramidal cells (Figure 6e). The remaining 20% of the change occurred within CA3 recurrent collaterals (Figure 6e). Altogether, these results demonstrate a significant decline in activity from reduced potentiation capacity.

Finally, we evaluated the effects of STDP impairment on the aggregate activity signals. We observed changes in in signal power commensurate with the changes in firing rate. Specifically, the dentate did not show any significant decreases in power (Figure 7a). In contrast, CA3 had a significant reduction in broadband power, affecting the theta, alpha, beta, and gamma bands ($p < .01$) (Figure 7b). Of these changes, the most important is the loss of theta power since this frequency band regulates the overall function of area CA3. CA1 also

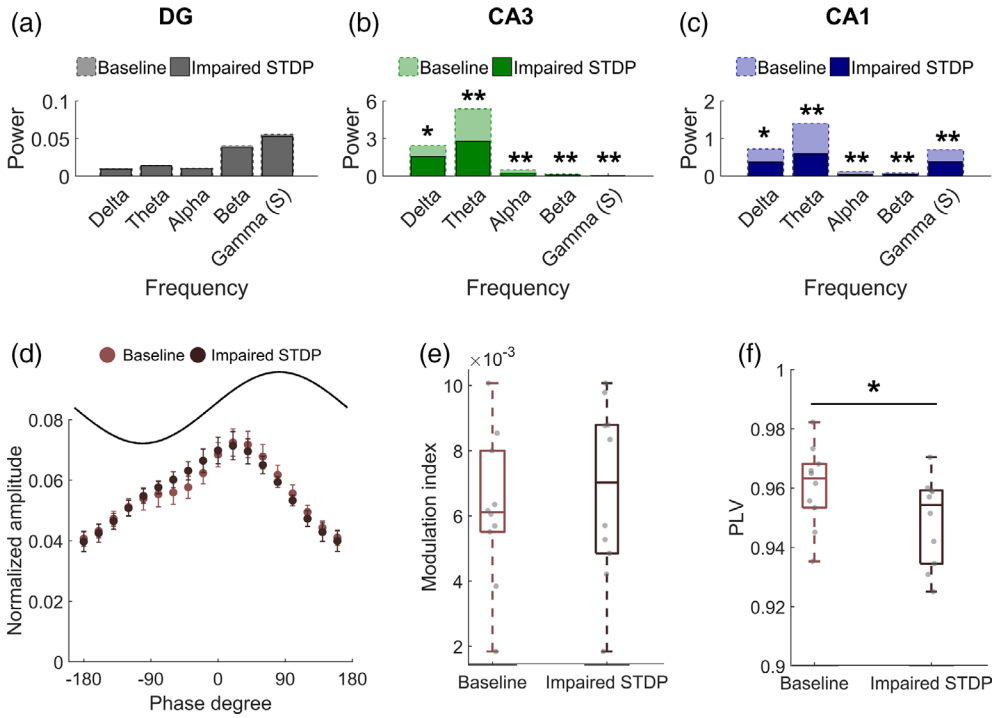

FIGURE 7 Impaired spike-timing-dependent plasticity (STDP) decreases broadband power in CA3 and CA1 but does not affect phase-amplitude coupling in CA1. (a) The dentate gyrus (DG) does not have significant changes in power after STDP impairment. (b) After injury, CA3 loses power in the theta, alpha, beta, and gamma bands but does not significantly decrease power in the delta band. (c) CA1 has significantly less power in the theta, beta, and gamma bands, with the largest decrease in theta (paired *t* test with Bonferroni correction; $^{*}p < .01$, $^{**}p <$ 1e-5 for (a–c)). (d) The phase-amplitude relationship does not change after STDP impairment. The sine wave shows an idealized theta waveform for comparison, and the peak of the gamma amplitude appears during the rising phase of theta. (e) There is no significant difference between the modulation index pre- and post-injury. (f) In contrast, there is a significant decrease in coherence between the theta rhythms of CA3 and CA1 after STDP impairment (paired *t* test; $p < .01$)

displayed significant loss of power in the theta, beta, and gamma bands ($p < .01$) (Figure 7c). Again, the theta and gamma bands are critical to the regional function, so these reductions are especially notable. Surprisingly, however, these shifts in power did not affect the PAC that is characteristic of CA1 (baseline: 6.2e-3 ± 2.3e-3 vs. STDP impairment: 6.7e-3 ± 3.0e-3; paired Student's *t* test; $p > .05$) (Figure 7d,e). There was a modest, yet significant, decline in phase coherence between the theta oscillations of CA3 and CA1 (baseline: 0.96 ± 0.01 vs. STDP impairment: 0.95 ± 0.16; paired Student's *t* test; $p < .01$) (Figure 7f). These results suggest that STDP impairment affected the longer-range communication between subregions more so than the local communication within a single area.

4 | DISCUSSION

In this work, we developed a neuronal network model of the hippocampus, including all three principal subregions of the DG, CA3, and CA1. We diligently incorporated physiological detail by relying on literature resources for electrophysiological and anatomical connectivity information. After developing individual neuron models and assembling the connectivity matrix, we measured and validated the overall network activity in several ways. First, we aimed to keep the average firing rate of each subtype within a literature-defined range. Beyond this raw measure of activity, the overall pattern of activity across the three subregions mimicked known frequency characteristics described in the literature. Specifically, CA3 has theta rhythms while CA1 mirrors these same theta rhythms and also exhibits gamma oscillations. Finally, the model displays phase coherence between theta signals in CA3 and CA1 as well as PAC, an additional higher-level feature, in CA1. Importantly, these features developed spontaneously without external constraints or explicitly encoding these frequencies, underscoring the need to study hippocampal subregions as an integrated system. Despite the size and level of complexity of the model, we were able to incorporate specific algorithms of HSP and STDP, broadening the future applications of the model. We demonstrated the importance of STDP within this work by revealing how a small alteration could impact network activity and behavior, reducing broadband power in CA3 and CA1 and phase coherence between CA3 and CA1.

In designing and constructing this model, we made several simplifications as we sought to balance biological fidelity and computational efficiency. First, we used a point neuron model, which neglects detailed morphology information, and simplified physical geometry, which lacks more complex lamellar structure. However, we find that the network activity recapitulates important features of firing rate and oscillation frequency, suggesting that these simplifications do not

detract from the validity of our model for assessing higher-level network features. Related to this simplification, we evaluated activity oscillations by aggregating simultaneous spikes across each subregion. We did not calculate a precise LFP or other electrophysiological correlate because such approximations are highly inaccurate for point neurons. As such, point neurons lack the compartmental morphology necessary to generate and measure dipoles, a prerequisite for producing an accurate LFP (Graben & Rodrigues, 2013; Mazzoni et al., 2015). Using compartmental neuron models was at odds with our goal of developing a detailed network model while retaining computational efficiency. Addressing the limitation of generating more accurate LFP correlates is outside the scope of this study, but others are working on this very subject (Camusas-Mesa & Quiroga, 2013; Einevoll et al., 2013; Graben & Rodrigues, 2013; Mazzoni et al., 2015). In addition to using point neurons for computational efficiency, we also used the Izhikevich neuron model to ensure the network model could run on a desktop computer. While other spiking neuron models have superior biophysical interpretability, the Izhikevich model is efficient and validated on neuron spiking patterns, the key feature for our analysis. Furthermore, the Izhikevich model is sufficiently adaptable in its formulation to simulate many types of neurons, so it is well suited to the heterogeneity of hippocampal neurons that we sought to incorporate in our model. Interestingly, although the single neuron models primarily display regular spiking behavior, more complex rhythms arise with synaptic connectivity across the network. Finally, this hippocampal network model remains less than full-scale with a limited number of neurons and receptors. To achieve a model with biological complexity and computational efficiency, we could not include all interneuron subtypes. Since many types of interneurons account for a nominal percentage of the overall cell population, the major subtypes specified in our model could accurately represent baseline regional activity. Still, to account for this limitation, we incorporated extra variance around interneuron parameters to represent a larger set of possible interneurons. In addition, this is a flexible platform and could easily be adapted to include an additional neuron subtype or receptor if the research question demanded it.

Aside from the limitations of the model, the method of injury (STDP impairment) is itself a simplification because the mechanisms underlying changes in plasticity after mild TBI are not well known. Although memory impairment is a common complaint for TBI patients, plasticity impairment remains an understudied mechanism of injury, especially mild injury. Previous work has demonstrated LTP impairment in both acute brain slices from animals after in vivo lateral fluid percussion injury and organotypic slice cultures after in vitro blast injury (Aungst et al., 2014; Effgen et al., 2016; Schwarzbach et al., 2006; Vogel et al., 2016, 2017). Aside from these assessments of LTP in hippocampal slice, the study of plasticity impairment has been limited. The LTP deficit is associated with reduced CaMKII expression and disruption of synaptic proteins like PSD-95 (Schwarzbach et al., 2006; Vogel et al., 2017). Our implementation amalgamates these effects into an overall reduction in synaptic potentiation. We chose to impair only the potentiation of synaptic strength in STDP, as injury does not generally impair the long-term depression in acute brain slices after TBI (Schwarzbach et al., 2006). Injury may also implicate other neural plasticity mechanisms, including HSP. While we did not explicitly incorporate a deficit in our HSP algorithm, we would expect such a change to support the results presented here. Since STDP has a shorter timescale than HSP, STDP is often the dominant mechanism when activity changes rapidly (Zenke et al., 2017). Our analysis was also limited to effects on neural activity; however, there is no direct link between the model and place fields, a measure of memory encoding, as detected with in vivo recording in behaving animals (Dombeck et al., 2010). Certainly, many other mechanisms might impact overall network plasticity. For instance, altering neurotransmission, intrinsic excitability of neurons, or the balance of excitation and inhibition in the network would alter the network firing rate and thereby intersect with STDP. Future work might address the interaction between the reduced capacity for synaptic potentiation and other injury mechanisms, such as cell loss or axonal degeneration. Since NMDA receptors are specifically associated with LTP induction (Madison et al., 1991; Malenka & Nicoll, 1993) and are mechanically sensitive to physical injury (Singh et al., 2012; Zhang et al., 1996), NMDA receptor damage might be a particularly interesting addition. Furthermore, LTP impairment may be an evolving condition, and this implementation consisted of a single intervention. While some electrophysiology studies have demonstrated deficits up to 28 days post-injury, LTP impairment may resolve depending on factors like the hippocampal subregion of interest (Aungst et al., 2014; White et al., 2017). Whether the circuit would regain preinjury activity levels if LTP impairment resolved is an open question.

The literature corroborates many of our initial findings in healthy networks. On a basic level, it is known that the DG is generally less active and less excitable than CA1 (Hsu, 2007; Paterno et al., 2017). Among the most compelling results is that the network supports both theta and gamma rhythms in CA1. These characteristic frequencies facilitate information transfer throughout the network (Canolty & Knight, 2010; Colgin, 2015; Sun et al., 2013). Not only do we find that our model generates these frequencies, but we also see theta-modulated gamma oscillations in CA1. PAC in which the amplitude of the gamma wave is coupled to the phase of the theta cycle is a well-studied phenomenon in CA1 (Belluscio et al., 2012; Canolty et al., 2006; Mormann et al., 2005; Soltesz & Deschenes, 1993). PAC putatively supports memory processing by facilitating the temporal organization of neural activity (Colgin, 2015; Fell & Axmacher, 2011). Recapitulating PAC in our model of the "healthy" hippocampus implies it would be a worthwhile tool to study how injury mechanisms contribute to changes in hippocampal function after injury. Moreover, theta frequency in the hippocampus is also known to modulate activity in the prefrontal cortex and to enable spatial memory in animals (Buzsáki, 2005; Colgin, 2013; Hanslmayr & Staudigl, 2014; Jin & Maren, 2015; Tamura et al., 2017), connecting our modeling results to spatial memory deficits after mild TBI (Folweiler et al., 2018; Paterno et al., 2017). Other efforts to explore how cross-frequency coupling varies dynamically by brain region and cognitive task have also begun to establish how forms of cross-frequency coupling like PAC could represent a functional link between network communication across

spatiotemporal scales (Canolty & Knight, 2010). Across the brain, cross-frequency coupling is associated with functions as wide-ranging as emotion (Schutter & Knyazev, 2011), motivation (Schroeder & Lakatos, 2009; Schutter & Knyazev, 2011), decision-making (Canolty & Knight, 2010; Schroeder & Lakatos, 2009), and attention (Lakatos et al., 2008; Schroeder & Lakatos, 2009)—all functions which may be affected by TBI.

Perhaps, the most striking effect of STDP impairment in our model is the broadband decrease in power observed in CA3 and CA1. Paterno et al. observed a similar reduction of broadband power in CA1 in acute hippocampal slices from animals that had undergone lateral fluid percussion injury (Paterno et al., 2016). Others have found that TBI attenuated specifically theta rhythms in the hippocampus of rats (Fedor et al., 2010; Lee et al., 2013, 2015). In patients with mild TBI, quantitative EEG analysis has revealed that injury symptoms are accompanied by changes in EEG power spectra (Modarres et al., 2017). Gosselin et al. found that concussed athletes had lower alpha power and higher delta power than controls did (Gosselin et al., 2009), suggesting an overall shift from higher to lower frequencies. Interestingly, the delta band is the only frequency band that was not significantly attenuated in CA3 or CA1 in our work. These results suggest a decrease in higher frequency power is an indicator of damage. This concept is also corroborated by earlier work in our lab on a model of network synchronization in which certain patterns of damage disrupted the network's ability to produce higher frequencies (Schumm et al., 2020).

The relative vulnerability of area CA3 of the hippocampus has long been a question of interest in the TBI field with some studies supporting the concept that CA3 is uniquely susceptible to injury while others contradict the idea (Cherubini & Miles, 2015; Mao, Elkin, et al., 2013; Witgen et al., 2005). Evidenced by reduced activity, power, and phase coherence, our results corroborate that the CA3 subregion is a weak point within the broader hippocampal circuitry when plasticity is impaired throughout the entire circuit. CA3 susceptibility is partially attributable to high activity owing to its structural (recurrent collaterals) and functional properties (lower inhibition), which raise the likelihood of plasticity-induced changes in synaptic strength as compared to other hippocampal subregions. Such characteristics make CA3 highly sensitive to alterations in the properties of STDP specifically and may also enhance the influence of this area across the hippocampus after TBI. In contrast, with its characteristic high inhibition, which remains unchanged by this injury mechanism, the DG has lower activity with less opportunity for STDP to interact, thereby contributing to overall stability under these conditions. Therefore, the DG appears largely unaffected by this form of plasticity impairment under baseline conditions. Together, these results indicate that specific injury mechanisms may differentially target some areas of the hippocampus more than others. Although area CA3 is challenging to study with traditional electrophysiological approaches, our model offers unique insight as to why it may be vulnerable to injury—namely high activity makes it prone to rapid synaptic changes that propagate downstream. Specifically, we showed decreased synaptic strength in CA3, and corresponding functional deficits manifest as reduced activity and power in both CA3 and CA1. Since the hippocampus and plasticity are crucial to the function of learning, we are interested in exploring network-based learning mechanisms with our model in future work. We anticipate that learning would put effects of damage into higher relief since exogenous stimulation would introduce an additional challenge to the network that it is likely unable to meet with potentiation deficits.

At a larger network scale, a decline of coherence between subregions without a decrease of PAC within a single subregion suggests that STDP impairment more strongly impacts long-range projections, which likely has functional implications. Since longer projections generally have longer propagation delays, distant synapses require precise modulation of spike timing to increase synaptic weight. With a global reduction in potentiation, distant synapses may no longer attain the requisite strength for coupling, contributing to aggregate decoupling with more remote regions. Although we are not aware of evidence showing this decline in coherence within the injured hippocampus, a number of functional MRI studies after TBI exhibit clear shifts in functional connectivity (Bonnelle et al., 2011; Mayer et al., 2011; Nakamura et al., 2009; Sours, George, et al., 2015; Venkatesan et al., 2015). Even though, the effects vary depending on factors such as injury severity, methodology, and brain regions of interest, many have found that injury decreases coherence of macroscale brain regions (Costanzo et al., 2014; Mayer et al., 2011; Palacios et al., 2017; Stevens et al., 2012). Furthermore, abnormalities in functional connectivity are correlated and predictive of symptom expression and cognitive deficits after traumatic injury (Mayer et al., 2011; Palacios et al., 2017; Stevens et al., 2012). With the effect on more distant connections, our work indicates that uniform impairment in plasticity can play an important role in rewiring broader circuitry within the brain. As such, our work raises the possibility that a synaptic scale pathology in TBI can have much broader consequences on brain function.

Finally, our work adds to past studies that examine other forms of neuropathology in TBI and begins to form a more comprehensive view of how different injury mechanisms perturb the function of damaged neural circuits. In our previous work on STDP and injury, we investigated how STDP can act as a homeostatic mechanism to restore baseline function in networks after injury, enabling the network to absorb damage and mitigate functional deficits (Gabrieli et al., 2020; Schumm et al., 2020). Potentiation impairment, as modeled here, would likely reduce the protective, or insulating, role that STDP provides against neurodegeneration. Likewise, deafferentation in a model of cortical circuitry can lead to the emergence of strong bursts of epileptiform activity (Volman et al., 2011). Introducing STDP may alleviate pathological bursting behavior, but this method of self-repair in the network would be limited under conditions of STDP impairment. Finally, STDP also significantly moderates the elevated activity that appears as a result of damage to mechanosensitive NMDA receptors (Gabrieli et al., 2021), and plasticity impairment would reduce or eliminate this activity-rate compensation across the network. Furthermore, in larger scale brain networks, STDP impairment may preferentially disrupt the coupling of more distant regions, and multiple injury mechanisms may co-occur across subregions of a single network. Considering the

interactions among several injury modalities suggests a general propensity to develop a less coherent circuit with more variable activity across the network after TBI. Although there is some evidence that mild TBI produces this type of change in network activity, future work that systematically examines the contribution of individual injury mechanisms is necessary to delineate whether these processes work in either an additive or a compensatory manner to affect cognitive processing.

Overall, this model comprises an adaptable framework for exploring the hippocampus in both health and disease. As such, it is poised to address many scientific questions about TBI, neural pathology, and neuroscience more broadly. Beyond TBI, many pathologies implicate the hippocampus, including Alzheimer's disease, schizophrenia, and post-traumatic stress disorder, among others (Small et al., 2011). Moreover, this work points toward an opportunity to link neuron-based network models and macroscale models of the whole human brain. Much like how the computational mechanics field has created models of the brain's mechanical response at different length scales (Ahmadzadeh et al., 2014; Finan et al., 2012; Mao, Zhang, et al., 2013), these multiscale models represent a means to connect injury mechanisms at the cellular/subcellular scale to overall impairments in cognitive function inferred through models of neural dynamics. In addition, this approach offers a tool for understanding how impairments emerge from several simultaneous injury mechanisms, a common occurrence in TBI and other acquired neurological disorders. In the long term, this work would facilitate a meaningful prediction of which therapies at the cellular level may be most beneficial for improving outcome after TBI and other neurological disorders.

ACKNOWLEDGMENTS

Funding was provided by grants by the Paul G. Allen Foundation and the NIH (RO1 NS088176). The authors would like to thank Sonia Kartha for careful review of the manuscript and Akiva Cohen for many helpful discussions about the physiology and function of the hippocampus. Parts of Figures 1 and 4 were created with BioRender.com.

DATA AVAILABILITY STATEMENT

Data sharing is not applicable to this article as no new data were created or analyzed in this study.

ORCID

Samantha N. Schumm https://orcid.org/0000-0003-4399-5362
David F. Meaney https://orcid.org/0000-0002-0954-4122

REFERENCES

Abhang, P. A., Gawali, B. W., & Mehrotra, S. C. (2016). Technological basics of EEG recording and operation of apparatus. In *Introduction to EEG- and speech-based emotion recognition* (pp. 19–50). Elsevier. https://doi.org/10.1016/b978-0-12-804490-2.00002-6

Ahmadzadeh, H., Smith, D. H., & Shenoy, V. B. (2014). Viscoelasticity of tau proteins leads to strain rate-dependent breaking of microtubules during axonal stretch injury: Predictions from a mathematical model. *Biophysical Journal*, *106*(5), 1123–1133. https://doi.org/10.1016/j.bpj.2014.01.024

Aika, Y., Ren, J. Q., Kosaka, K., & Kosaka, T. (1994). Quantitative analysis of GABA-like-immunoreactive and parvalbumin-containing neurons in the CA1 region of the rat hippocampus using a stereological method, the disector. *Experimental Brain Research*, *99*(2), 267–276. https://doi.org/10.1007/BF00239593

Albensi, B. C., & Janigro, D. (2003). Traumatic brain injury and its effects on synaptic plasticity. *Brain Injury*, *17*(8), 653–663. https://doi.org/10.1080/0269905031000107142

Albensi, B. C., Sullivan, P. G., Thompson, M. B., Scheff, S. W., & Mattson, M. P. (2000). Cyclosporin ameliorates traumatic brain-injury-induced alterations of hippocampal synaptic plasticity. *Experimental Neurology*, *162*(2), 385–389. https://doi.org/10.1006/exnr.1999.7338

Andersen, P., Soleng, A. F., & Raastad, M. (2000). The hippocampal lamella hypothesis revisited. *Brain Research*, *886*(1–2), 165–171. https://doi.org/10.1016/s0006-8993(00)02991-7

Aungst, S. L., Kabadi, S. V., Thompson, S. M., Stoica, B. A., & Faden, A. I. (2014). Repeated mild traumatic brain injury causes chronic neuroinflammation, changes in hippocampal synaptic plasticity, and associated cognitive deficits. *Journal of Cerebral Blood Flow and Metabolism*, *34*(7), 1223–1232. https://doi.org/10.1038/jcbfm.2014.75

Battaglia, F. P., Benchenane, K., Sirota, A., Pennartz, C. M. A., & Wiener, S. I. (2011). The hippocampus: Hub of brain network communication for memory. *Trends in Cognitive Sciences*, *15*(7), 310–318. https://doi.org/10.1016/j.tics.2011.05.008

Belluscio, M. A., Mizuseki, K., Schmidt, R., Kempter, R., & Buzsáki, G. (2012). Cross-frequency phase-phase coupling between theta and gamma oscillations in the hippocampus. *Journal of Neuroscience*, *32*(2), 423–435. https://doi.org/10.1523/JNEUROSCI.4122-11.2012

Bezaire, M. J., Raikov, I., Burk, K., Vyas, D., & Soltesz, I. (2016). Interneuronal mechanisms of hippocampal theta oscillations in a full-scale model of the rodent CA1 circuit. *eLife*, *5*(DECEMBER2016), 1–106. https://doi.org/10.7554/eLife.18566

Bezaire, M. J., & Soltesz, I. (2013). Quantitative assessment of CA1 local circuits: Knowledge base for interneuron-pyramidal cell connectivity. *Hippocampus*, *23*(9), 751–785. https://doi.org/10.1002/hipo.22141

Bigler, E. D., & Maxwell, W. L. (2012). Neuropathology of mild traumatic brain injury: Relationship to neuroimaging findings. *Brain Imaging and Behavior*, *6*(2), 108–136. https://doi.org/10.1007/s11682-011-9145-0

Bird, C. M., & Burgess, N. (2008). The hippocampus and memory: Insights from spatial processing. *Nature Reviews. Neuroscience*, *9*(3), 182–194. https://doi.org/10.1038/nrn2335

Blennow, K., Brody, D. L., Kochanek, P. M., Levin, H., McKee, A., Ribbers, G. M., Yaffe, K., & Zetterberg, H. (2016). Traumatic brain injuries. *Nature Reviews Disease Primers*, *2*, 16084. https://doi.org/10.1038/nrdp.2016.84

Bonnelle, V., Leech, R., Kinnunen, K. M., Ham, T. E., Beckmann, C. F., De Boissezon, X., … Sharp, D. J. (2011). Default mode network connectivity predicts sustained attention deficits after traumatic brain injury. *Journal of Neuroscience*, *31*(38), 13442–13451. https://doi.org/10.1523/JNEUROSCI.1163-11.2011

Buzsáki, G. (2005). Theta rhythm of navigation: Link between path integration and landmark navigation, episodic and semantic memory. *Hippocampus*, *15*, 827–840. https://doi.org/10.1002/hipo.20113

Camusas-Mesa, L. A., & Quiroga, R. Q. (2013). A detailed and fast model of extracellular recordings. *Neural Computation*, *25*, 1191–1212. https://doi.org/10.1162/NECO

Cancelliere, C., Coronado, V. G., Taylor, C. A., & Xu, L. (2017). Epidemiology of isolated versus nonisolated mild traumatic brain injury treated in emergency departments in the United States, 2006-2012: Sociodemographic characteristics. *Journal of Head Trauma Rehabilitation*, *32*(4), E37–E46. https://doi.org/10.1097/HTR.0000000000000260

Canolty, R. T., Edwards, E., Dalal, S. S., Soltani, M., Nagarajan, S. S., Kirsch, H. E., … Knight, R. T. (2006). High gamma power is phase-locked to theta oscillations in human neocortex. *Science*, *313*(5793), 1626–1628. https://doi.org/10.1126/science.1128115

Canolty, R. T., & Knight, R. T. (2010). The functional role of cross-frequency coupling. *Trends in Cognitive Sciences*, *14*(11), 506–515. https://doi.org/10.1016/j.tics.2010.09.001

Canteras, N. S., & Swanson, L. W. (1992). Projections of the ventral subiculum to the amygdala, septum, and hypothalamus: A PHAL anterograde tract-tracing study in the rat. *The Journal of Comparative Neurology*, *324*(2), 180–194. https://doi.org/10.1002/cne.903240204

Caporale, N., & Dan, Y. (2008). Spike timing-dependent plasticity: A Hebbian learning rule. *Annual Review of Neuroscience*, *31*, 25–46. https://doi.org/10.1146/annurev.neuro.31.060407.125639

Chavlis, S., Petrantonakis, P. C., & Poirazi, P. (2017). Dendrites of dentate gyrus granule cells contribute to pattern separation by controlling sparsity. *Hippocampus*, *27*(1), 89–110. https://doi.org/10.1002/hipo.22675

Chen, T. W., Wardill, T. J., Sun, Y., Pulver, S. R., Renninger, S. L., Baohan, A., … Kim, D. S. (2013). Ultrasensitive fluorescent proteins for imaging neuronal activity. *Nature*, *499*(7458), 295–300. https://doi.org/10.1038/nature12354

Cherubini, E., & Miles, R. (2015). The CA3 region of the hippocampus: How is it? What is it for? How does it do it? *Frontiers in Cellular Neuroscience*, *9*, 19. https://doi.org/10.3389/fncel.2015.00019

Cohen, A. S., Pfister, B. J., Schwarzbach, E., Sean Grady, M., Goforth, P. B., & Satin, L. S. (2007). Injury-induced alterations in CNS electrophysiology. *Progress in Brain Research*, *161*, 143–169. https://doi.org/10.1016/S0079-6123(06)61010-8

Colgin, L. L. (2013). Mechanisms and functions of theta rhythms. *Annual Review of Neuroscience*, *36*(1), 295–312. https://doi.org/10.1146/annurev-neuro-062012-170330

Colgin, L. L. (2015). Theta-gamma coupling in the entorhinal-hippocampal system. *Current Opinion in Neurobiology*, *31*, 45–50. https://doi.org/10.1016/j.conb.2014.08.001

Colgin, L. L. (2016). Rhythms of the hippocampal network. *Nature Reviews Neuroscience*, *17*(4), 239–249. https://doi.org/10.1038/nrn.2016.21

Colgin, L. L., Denninger, T., Fyhn, M., Hafting, T., Bonnevie, T., Jensen, O., … Moser, E. I. (2009). Frequency of gamma oscillations routes flow of information in the hippocampus. *Nature*, *462*, 353–357. https://doi.org/10.1038/nature08573

Costanzo, M. E., Chou, Y.-Y., Leaman, S., Pham, D. L., Keyser, D., Nathan, D. E., … Roy, M. J. (2014). Connecting combat-related mild traumatic brain injury with posttraumatic stress disorder symptoms through brain imaging. *Neuroscience Letters*, *577*, 11–15. https://doi.org/10.1016/j.neulet.2014.05.054

Cutsuridis, V., Cobb, S., & Graham, B. P. (2010). Encoding and retrieval in a model of the hippocampal CA1 microcircuit. *Hippocampus*, *20*(3), 423–446. https://doi.org/10.1002/hipo.20661

Dombeck, D. A., Harvey, C. D., Tian, L., Looger, L. L., & Tank, D. W. (2010). Functional imaging of hippocampal place cells at cellular resolution during virtual navigation. *Nature Neuroscience*, *13*(11), 1433–1440. https://doi.org/10.1038/nn.2648

Dyhrfjeld-Johnsen, J., Santhakumar, V., Morgan, R. J., Huerta, R., Tsimring, L., & Soltesz, I. (2007). Topological determinants of epileptogenesis in large-scale structural and functional models of the dentate gyrus derived from experimental data. *Journal of Neurophysiology*, *97*(2), 1566–1587. https://doi.org/10.1152/jn.00950.2006

Effenberger, F., Jost, J., & Levina, A. (2015). Self-organization in balanced state networks by STDP and homeostatic plasticity. *PLoS Computational Biology*, *11*(9), e1004420. https://doi.org/10.1371/journal.pcbi.1004420

Effgen, G. B., Ong, T., Nammalwar, S., Ortuño, A. I., Meaney, D. F., Bass, C. R. D., & Morrison, B. (2016). Primary blast exposure increases hippocampal vulnerability to subsequent exposure: Reducing long-term potentiation. *Journal of Neurotrauma*, *33*(20), 1901–1912. https://doi.org/10.1089/neu.2015.4327

Einevoll, G. T., Kayser, C., Logothetis, N. K., & Panzeri, S. (2013). Modelling and analysis of local field potentials for studying the function of cortical circuits. *Nature Reviews Neuroscience*, *14*, 770–785. https://doi.org/10.1038/nrn3599

Fanselow, M. S., & Dong, H.-W. (2010). Are the dorsal and ventral hippocampus functionally distinct structures? *Neuron*, *65*(1), 7–19. https://doi.org/10.1016/j.neuron.2009.11.031

Fedor, M., Berman, R. F., Muizelaar, J. P., & Lyeth, B. G. (2010). Hippocampal theta dysfunction after lateral fluid percussion injury. *Journal of Neurotrauma*, *27*(9), 1605–1615. https://doi.org/10.1089/neu.2010.1370

Fell, J., & Axmacher, N. (2011). Local field potential the role of phase synchronization in memory processes. *Nature Reviews Neuroscience*, *12*, 105–118. https://doi.org/10.1038/nrn2979

Ferster, D., & Jagadeesh, B. (1992). EPSP-IPSP interactions in cat visual cortex studied with in vivo whole-cell patch recording. *Journal of Neuroscience*, *12*(4), 1262–1274.

Finan, J. D., Elkin, B. S., Pearson, E. M., Kalbian, I. L., & Morrison, B. (2012). Viscoelastic properties of the rat brain in the sagittal plane: Effects of anatomical structure and age. *Annals of Biomedical Engineering*, *40*(1), 70–78. https://doi.org/10.1007/s10439-011-0394-2

Fink, C. G., Gliske, S., Catoni, N., & Stacey, W. C. (2015). Network mechanisms generating abnormal and normal hippocampal high-frequency oscillations: A computational analysis. *ENeuro*, *2*(3), 24–39. https://doi.org/10.1523/ENEURO.0024-15.2015

Folweiler, K. A., Samuel, S., Metheny, H. E., & Cohen, A. S. (2018). Diminished dentate gyrus filtering of cortical input leads to enhanced area CA3 excitability after mild traumatic brain injury. *Journal of Neurotrauma*, *35*(11), 1304–1317. https://doi.org/10.1089/neu.2017.5350

Gabrieli, D., Schumm, S. N., Vigilante, N. F., & Meaney, D. F. (2021). NMDA receptor alterations after mild traumatic brain injury induce deficits in memory acquisition and recall. *Neural Computation*, *33*, 1–29. https://doi.org/10.1162/neco_a_01343

Gabrieli, D., Schumm, S. N., Vigilante, N. F., Parvesse, B., & Meaney, D. F. (2020). Neurodegeneration exposes firing rate dependent effects on oscillation dynamics in computational neural networks. *PLoS One*, *15*(9), e0234749. https://doi.org/10.1371/journal.pone.0234749

Gosselin, N., Lassonde, M., Petit, D., Leclerc, S., Mongrain, V., Collie, A., & Montplaisir, J. (2009). Sleep following sport-related concussions. *Sleep Medicine*, *10*(1), 35–46. https://doi.org/10.1016/j.sleep.2007.11.023

Graben, P. B., & Rodrigues, S. (2013). A biophysical observation model for field potentials of networks of leaky integrate-and-fire neurons. *Frontiers in Computational Neuroscience*, *JAN*, 1–13. https://doi.org/10.3389/fncom.2012.00100

Hanslmayr, S., & Staudigl, T. (2014). How brain oscillations form memories—A processing based perspective on oscillatory subsequent memory effects. *NeuroImage*, *85*, 648–655. https://doi.org/10.1016/j.neuroimage.2013.05.121

Harvey, C. D., Collman, F., Dombeck, D. A., & Tank, D. W. (2009). Intracellular dynamics of hippocampal place cells during virtual navigation. *Nature*, *461*(7266), 941–946. https://doi.org/10.1038/nature08499

Hiploylee, C., Dufort, P. A., Davis, H. S., Wennberg, R. A., Tartaglia, M. C., Mikulis, D., … Tator, C. H. (2017). Longitudinal study of postconcussion syndrome: Not everyone recovers. *Journal of Neurotrauma*, *34*, 1511–1523. https://doi.org/10.1089/neu.2016.4677

Hsu, D. (2007). The dentate gyrus as a filter or gate: A look back and a look ahead. *Progress in Brain Research*, *163*, 601–613. https://doi.org/10.1016/S0079-6123(07)63032-5

Hülsemann, M. J., Naumann, E., & Rasch, B. (2019). Quantification of phase-amplitude coupling in neuronal oscillations: Comparison of phase-locking value, mean vector length, modulation index, and generalized-linear-modeling-cross-frequency-coupling. *Frontiers in Neuroscience*, *13*(June), 573. https://doi.org/10.3389/fnins.2019.00573

Hummos, A., & Nair, S. S. (2017). An integrative model of the intrinsic hippocampal theta rhythm. *PLoS One*, *12*(8), e0182648. https://doi.org/10.1371/journal.pone.0182648

Hyder, A. A., Wunderlich, C. A., Puvanachandra, P., Gururaj, G., & Kobusingye, O. C. (2007). The impact of traumatic brain injuries: A global perspective. *NeuroRehabilitation*, *22*(5), 341–353. https://doi.org/10.3233/nre-2007-22502

Izhikevich, E. M. (2003). Simple model of spiking neurons. *IEEE Transactions on Neural Networks*, *14*(6), 1569–1572. https://doi.org/10.1109/TNN.2003.820440

Izhikevich, E. M. (2010). *Dynamical systems in neuroscience*. The MIT Press. https://doi.org/10.7551/mitpress/2526.001.0001

Izhikevich, E. M., & Edelman, G. M. (2008). Large-scale model of mammalian thalamocortical systems. *Proceedings of the National Academy of Sciences of the United States of America*, *105*(9), 3593–3598. https://doi.org/10.1073/pnas.0712231105

Jin, J., & Maren, S. (2015). Prefrontal-hippocampal interactions in memory and emotion. *Frontiers in Systems Neuroscience*, *9*, 170. https://doi.org/10.3389/fnsys.2015.00170

Koch, C. (2004). *Biophysics of computation: Information processing in single neurons*. Oxford University Press. https://doi.org/10.1086/394197

Kotapka, M. J., Graham, D. I., Adams, J. H., & Gennarelli, T. A. (1994). Hippocampal pathology in fatal human head injury without high intracranial pressure. *Journal of Neurotrauma*, *11*(3), 317–324. https://doi.org/10.1089/neu.1994.11.317

Kress, G. J., Dowling, M. J., Meeks, J. P., & Mennerick, S. (2008). High threshold, proximal initiation, and slow conduction velocity of action potentials in dentate granule neuron mossy fibers. *Journal of Neurophysiology*, *100*(1), 281–291. https://doi.org/10.1152/jn.90295.2008

Lachaux, J. P., Rodriguez, E., Martinerie, J., & Varela, F. J. (1999). Measuring phase synchrony in brain signals. *Human Brain Mapping*, *8*(4), 194–208. https://doi.org/10.1002/(sici)1097-0193(1999)8:4<194::aid-hbm4>3.0.co;2-c

Lakatos, P., Karmos, G., Mehta, A. D., Ulbert, I., & Schroeder, C. E. (2008). Entrainment of neuronal oscillations as a mechanism of attentional selection. *Science*, *320*(5872), 110–113. https://doi.org/10.1126/science.1154735

Lee, D. J., Gurkoff, G. G., Izadi, A., Berman, R. F., Ekstrom, A. D., Muizelaar, J. P., … Shahlaie, K. (2013). Medial septal nucleus theta frequency deep brain stimulation improves spatial working memory after traumatic brain injury. *Journal of Neurotrauma*, *30*(2), 131–139. https://doi.org/10.1089/neu.2012.2646

Lee, D. J., Gurkoff, G. G., Izadi, A., Seidl, S. E., Echeverri, A., Melnik, M., … Shahlaie, K. (2015). Septohippocampal neuromodulation improves cognition after traumatic brain injury. *Journal of Neurotrauma*, *32*(22), 1822–1832. https://doi.org/10.1089/neu.2014.3744

Lein, P. J., Barnhart, C. D., & Pessah, I. N. (2011). Acute hippocampal slice preparation and hippocampal slice cultures. *Methods in Molecular Biology*, *758*, 115–134. https://doi.org/10.1007/978-1-61779-170-3_8

Lu, J. T., Li, C. Y., Zhao, J. P., Poo, M. M., & Zhang, X. H. (2007). Spike-timing-dependent plasticity of neocortical excitatory synapses on inhibitory interneurons depends on target cell type. *Journal of Neuroscience*, *27*(36), 9711–9720. https://doi.org/10.1523/JNEUROSCI.2513-07.2007

Madison, D. V., Malenka, R. C., & Nicoll, R. A. (1991). Mechanisms underlying long-term potentiation of synaptic transmission. *Annual Review of Neuroscience*, *14*(1), 379–397. https://doi.org/10.1146/annurev.ne.14.030191.002115

Malenka, R. C., & Nicoll, R. A. (1993). NMDA-receptor-dependent synaptic plasticity: Multiple forms and mechanisms. *Trends in Neurosciences*, *16*(12), 521–527. https://doi.org/10.1016/0166-2236(93)90197-T

Malerba, P., Krishnan, G. P., Fellous, J.-M., & Bazhenov, M. (2016). Hippocampal CA1 ripples as inhibitory transients. *PLoS Computational Biology*, *12*(4), e1004880. https://doi.org/10.1371/journal.pcbi.1004880

Mao, H., Elkin, B. S., Genthikatti, V. V., Morrison, B., & Yang, K. H. (2013). Why is CA3 more vulnerable than CA1 in experimental models of controlled cortical impact-induced brain injury? *Journal of Neurotrauma*, *30*(17), 1521–1530. https://doi.org/10.1089/neu.2012.2520

Mao, H., Zhang, L., Jiang, B., Genthikatti, V. V., Jin, X., Zhu, F., … Yang, K. H. (2013). Development of a finite element human head model partially validated with thirty five experimental cases. *Journal of Biomechanical Engineering*, *135*(11), 111002. https://doi.org/10.1115/1.4025101

Martin, E. M., Lu, W. C., Helmick, K., French, L., & Warden, D. L. (2008). Traumatic brain injuries sustained in the Afghanistan and Iraq wars. *Journal of Trauma Nursing*, *15*(3), 94–99. https://doi.org/10.1097/01.jtn.0000337149.29549.28

Mayer, A. R., Mannell, M. V., Ling, J., Gasparovic, C., & Yeo, R. A. (2011). Functional connectivity in mild traumatic brain injury. *Human Brain Mapping*, *32*(11), 1825–1835. https://doi.org/10.1002/hbm.21151

Mazzoni, A., Lindén, H., Cuntz, H., Lansner, A., Panzeri, S., & Einevoll, G. T. (2015). Computing the local field potential (LFP) from integrate-and-fire network models. *PLoS Computational Biology*, *11*(12), e1004584. https://doi.org/10.1371/journal.pcbi.1004584

McAllister, T. W. (2011). Neurobiological consequences of traumatic brain injury. *Dialogues in Clinical Neuroscience*, *13*(3), 287–300.

Meeks, J. P., & Mennerick, S. (2007). Action potential initiation and propagation in CA3 pyramidal axons. *Journal of Neurophysiology*, *97*(5), 3460–3472. https://doi.org/10.1152/jn.01288.2006

Miles, R., Traub, R. D., & Wong, R. K. S. (1988). Spread of synchronous firing in longitudinal slices from the CA3 region of the hippocampus. *Journal of Neurophysiology*, *60*(4), 1481–1496. https://doi.org/10.1152/jn.1988.60.4.1481

Modarres, M. H., Kuzma, N. N., Kretzmer, T., Pack, A. I., & Lim, M. M. (2017). EEG slow waves in traumatic brain injury: Convergent findings in mouse and man. *Neurobiology of Sleep and Circadian Rhythms*, *2*, 59–70. https://doi.org/10.1016/j.nbscr.2016.06.001

Morales, D. M. M., Marklund, N., Lebold, D., Thompson, H. J. J., Pitkanen, A., Maxwell, W. L. L., … McIntosh, T. K. K. (2005). Experimental models of traumatic brain injury: Do we really need to build a better mousetrap? *Neuroscience*, *136*(4), 971–989. https://doi.org/10.1016/j.neuroscience.2005.08.030

Morgan, R. J., Santhakumar, V., & Soltesz, I. (2007). Modeling the dentate gyrus. *Progress in Brain Research*, *163*, 639–658. https://doi.org/10.1016/S0079-6123(07)63035-0

Mormann, F., Fell, J., Axmacher, N., Weber, B., Lehnertz, K., Elger, C. E., & Fernández, G. (2005). Phase/amplitude reset and theta-gamma interaction in the human medial temporal lobe during a continuous word recognition memory task. *Hippocampus*, *15*(7), 890–900. https://doi.org/10.1002/hipo.20117

Myers, C. E., & Scharfman, H. E. (2011). Pattern separation in the dentate gyrus: A role for the CA3 backprojection. *Hippocampus*, *21*(11), 1190–1215. https://doi.org/10.1002/hipo.20828

Nakamura, T., Hillary, F. G., & Biswal, B. B. (2009). Resting network plasticity following brain injury. *PLoS One*, *4*(12), e8220. https://doi.org/10.1371/journal.pone.0008220

Neymotin, S. A., Lazarewicz, M. T., Sherif, M., Contreras, D., Finkel, L. H., & Lytton, W. W. (2011). Ketamine disrupts theta modulation of gamma in a computer model of hippocampus. *Journal of Neuroscience*, *31*(32), 11733–11743. https://doi.org/10.1523/JNEUROSCI.0501-11.2011

O'Mara, S. (2005). The subiculum: What it does, what it might do, and what neuroanatomy has yet to tell us. *Journal of Anatomy*, *207*, 271–282. https://doi.org/10.1111/j.1469-7580.2005.00446.x

Palacios, E. M., Yuh, E. L., Chang, Y. S., Yue, J. K., Schnyer, D. M., Okonkwo, D. O., … Mukherjee, P. (2017). Resting-state functional connectivity alterations associated with six-month outcomes in mild traumatic brain injury. *Journal of Neurotrauma*, *34*(8), 1546–1557. https://doi.org/10.1089/neu.2016.4752

Paterno, R., Folweiler, K. A., & Cohen, A. S. (2017). Pathophysiology and treatment of memory dysfunction after traumatic brain injury. *Current*

Neurology and Neuroscience Reports, *17*(7), 52. https://doi.org/10.1007/s11910-017-0762-x

Paterno, R., Metheny, H., Xiong, G., Elkind, J., & Cohen, A. S. (2016). Mild traumatic brain injury decreases broadband power in area CA1. *Journal of Neurotrauma*, *33*, 1645–1649. https://doi.org/10.1089/neu.2015.4107

Raghupathi, R. (2004). Cell death mechanisms following traumatic brain injury. *Brain Pathology*, *14*(2), 215–222. https://doi.org/10.1111/j.1750-3639.2004.tb00056.x

Rutishauser, U., Ross, I. B., Mamelak, A. N., & Schuman, E. M. (2010). Human memory strength is predicted by theta-frequency phase-locking of single neurons. *Nature*, *464*(7290), 903–907. https://doi.org/10.1038/nature08860

Sanjay, M., Neymotin, S. A., & Krothapalli, S. B. (2015). Impaired dendritic inhibition leads to epileptic activity in a computer model of CA3. *Hippocampus*, *25*(11), 1336–1350. https://doi.org/10.1002/hipo.22440

Santhakumar, V., Aradi, I., & Soltesz, I. (2005). Role of mossy fiber sprouting and mossy cell loss in hyperexcitability: A network model of the dentate gyrus incorporating cell types and axonal topography. *Journal of Neurophysiology*, *93*, 437–453. https://doi.org/10.1152/jn.00777.2004

Santhakumar, V., Ratzliff, A. D. H., Jeng, J., Toth, Z., & Soltesz, I. (2001). Long-term hyperexcitability in the hippocampus after experimental head trauma. *Annals of Neurology*, *50*(6), 708–717. https://doi.org/10.1002/ana.1230

Schroeder, C. E., & Lakatos, P. (2009). Low-frequency neuronal oscillations as instruments of sensory selection. *Trends in Neurosciences*, *32*(1), 9–18. https://doi.org/10.1016/j.tins.2008.09.012

Schumm, S. N., Gabrieli, D., & Meaney, D. F. (2020). Neuronal degeneration impairs rhythms between connected microcircuits. *Frontiers in Computational Neuroscience*, *14*, 18. https://doi.org/10.3389/fncom.2020.00018

Schutter, D. J. L. G., & Knyazev, G. G. (2011). Cross-frequency coupling of brain oscillations in studying motivation and emotion. *Motivation and Emotion*, *36*, 46–54. https://doi.org/10.1007/s11031-011-9237-6

Schwarzbach, E., Bonislawski, D. P., Xiong, G., & Cohen, A. S. (2006). Mechanisms underlying the inability to induce area CA1 LTP in the mouse after traumatic brain injury. *Hippocampus*, *16*(6), 541–550. https://doi.org/10.1002/hipo.20183

Singh, P., Doshi, S., Spaethling, J. M., Hockenberry, A. J., Patel, T. P., Geddes-Klein, D. M., … Meaney, D. F. (2012). *N* -methyl-d-aspartate receptor mechanosensitivity is governed by C terminus of NR2B subunit. *Journal of Biological Chemistry*, *287*(6), 4348–4359. https://doi.org/10.1074/jbc.M111.253740

Small, S. A., Schobel, S. A., Buxton, R. B., Witter, M. P., & Barnes, C. A. (2011). A pathophysiological framework of hippocampal dysfunction in ageing and disease. *Nature Reviews Neuroscience*, *12*(10), 585–601. https://doi.org/10.1038/nrn3085

Soltesz, I., & Deschenes, M. (1993). Low- and high-frequency membrane potential oscillations during theta activity in CA1 and CA3 pyramidal neurons of the rat hippocampus under ketamine-xylazine anesthesia. *Journal of Neurophysiology*, *70*(1), 97–115. https://doi.org/10.1152/jn.1993.70.1.97

Sours, C., George, E. O., Zhuo, J., Roys, S., & Gullapalli, R. P. (2015). Hyperconnectivity of the thalamus in during early stages following mild traumatic brain injury. *Brain Imaging and Behavior*, *9*(3), 550–563. https://doi.org/10.1007/s11682-015-9424-2

Sours, C., Zhuo, J., Roys, S., Shanmuganathan, K., & Gullapalli, R. P. (2015). Disruptions in resting state functional connectivity and cerebral blood flow in mild traumatic brain injury patients. *PLoS One*, *10*(8), e0134019. https://doi.org/10.1371/journal.pone.0134019

Stam, C. J. (2014). Modern network science of neurological disorders. *Nature Reviews Neuroscience*, *15*(10), 683–695. https://doi.org/10.1038/nrn3801

Stanley, D. A., Talathi, S. S., Parekh, M. B., Cordiner, D. J., Zhou, J., Mareci, T. H., … Carney, P. R. (2013). Phase shift in the 24-hour rhythm of hippocampal EEG spiking activity in a rat model of temporal lobe epilepsy. *Journal of Neurophysiology*, *110*(5), 1070–1086. https://doi.org/10.1152/jn.00911.2012

Stevens, M. C., Lovejoy, D., Kim, J., Oakes, H., Kureshi, I., & Witt, S. T. (2012). Multiple resting state network functional connectivity abnormalities in mild traumatic brain injury. *Brain Imaging and Behavior*, *6*(2), 293–318. https://doi.org/10.1007/s11682-012-9157-4

Strange, B. A., Witter, M. P., Lein, E. S., & Moser, E. I. (2014). Functional organization of the hippocampal longitudinal axis. *Nature Reviews Neuroscience*, *15*(10), 655–669. https://doi.org/10.1038/nrn3785

Strüber, M., Sauer, J.-F., Jonas, P., & Bartos, M. (2017). Distance-dependent inhibition facilitates focality of gamma oscillations in the dentate gyrus. *Nature Communications*, *8*(1), 758. https://doi.org/10.1038/s41467-017-00936-3

Sun, X. R., Badura, A., Pacheco, D. A., Lynch, L. A., Schneider, E. R., Taylor, M. P., … Neher, E. (2013). Fast GCaMPs for improved tracking of neuronal activity. *Nature Communications*, *4*, 1–7. https://doi.org/10.1038/ncomms3170

Tamura, M., Spellman, T. J., Rosen, A. M., Gogos, J. A., & Gordon, J. A. (2017). Hippocampal-prefrontal theta-gamma coupling during performance of a spatial working memory task. *Nature Communications*, *8*, 2182. https://doi.org/10.1038/s41467-017-02108-9

Tejada, J., Garcia-Cairasco, N., & Roque, A. C. (2014). Combined role of seizure-induced dendritic morphology alterations and spine loss in newborn granule cells with mossy fiber sprouting on the hyperexcitability of a computer model of the dentate gyrus. *PLoS Computational Biology*, *10*(5), e1003601. https://doi.org/10.1371/journal.pcbi.1003601

Tetzlaff, C., Kolodziejski, C., Timme, M., & Wörgötter, F. (2011). Synaptic scaling in combination with many generic plasticity mechanisms stabilizes circuit connectivity. *Frontiers in Computational Neuroscience*, *5*, 47. https://doi.org/10.3389/fncom.2011.00047

Tort, A. B. L., Kramer, M. A., Thorn, C., Gibson, D. J., Kubota, Y., Graybiel, A. M., & Kopell, N. J. (2008). Dynamic cross-frequency couplings of local field potential oscillations in rat striatum and hippocampus during performance of a T-maze task. *Proceedings of the National Academy of Sciences of the United States of America*, *105*(51), 20517–20522. https://doi.org/10.1073/pnas.0810524105

Treves, A., & Rolls, E. T. (1994). Computational analysis of the role of the hippocampus in memory. *Hippocampus*, *4*(3), 374–391. https://doi.org/10.1002/hipo.450040319

Tripathy, S. J., Savitskaya, J., Burton, S. D., Urban, N. N., & Gerkin, R. C. (2014). NeuroElectro: A window to the world's neuron electrophysiology data. *Frontiers in Neuroinformatics*, *8*(APR), 40. https://doi.org/10.3389/fninf.2014.00040

Turrigiano, G. G., Leslie, K. R., Desai, N. S., Rutherford, L. C., & Nelson, S. B. (1998). Activity-dependent scaling of quantal amplitude in neocortical neurons. *Nature*, *391*(6670), 892–896. https://doi.org/10.1038/36103

Turrigiano, G. G., & Nelson, S. B. (2004). Homeostatic plasticity in the developing nervous system. *Nature Reviews Neuroscience*, *5*(2), 97–107. https://doi.org/10.1038/nrn1327

Venkatesan, U. M., Dennis, N. A., & Hillary, F. G. (2015). Chronology and chronicity of altered resting-state functional connectivity after traumatic brain injury. *Journal of Neurotrauma*, *32*(4), 252–264. https://doi.org/10.1089/neu.2013.3318

Vogel, E. W., Effgen, G. B., Patel, T. P., Meaney, D. F., Bass, C. R., & Morrison, B. (2016). Isolated primary blast inhibits long-term potentiation in organotypic hippocampal slice cultures. *Journal of Neurotrauma*, *33*(7), 652–661. https://doi.org/10.1089/neu.2015.4045

Vogel, E. W., Rwema, S. H., Meaney, D. F., Bass, C. R. Q., & Morrison, B. (2017). Primary blast injury depressed hippocampal long-term potentiation through disruption of synaptic proteins. *Journal of Neurotrauma*, *34*(5), 1063–1073. https://doi.org/10.1089/neu.2016.4578

Volman, V., Bazhenov, M., & Sejnowski, T. J. (2011). Pattern of trauma determines the threshold for epileptic activity in a model of cortical deafferentation. *Proceedings of the National Academy of Sciences of the United States of America*, *108*(37), 15402–15407. https://doi.org/10.1073/pnas.1112066108

Wheeler, D. W., White, C. M., Rees, C. L., Komendantov, A. O., Hamilton, D. J., & Ascoli, G. A. (2015). Hippocampome.org: A knowledge base of neuron types in the rodent hippocampus. *eLife*, *4* (September2015), e09960. https://doi.org/10.7554/eLife.09960

White, E. R., Pinar, C., Bostrom, C. A., Meconi, A., & Christie, B. R. (2017). Mild traumatic brain injury produces long-lasting deficits in synaptic plasticity in the female juvenile hippocampus. *Journal of Neurotrauma*, *34*(5), 1111–1123. https://doi.org/10.1089/neu.2016.4638

Witgen, B. M., Lifshitz, J., Smith, M. L., Schwarzbach, E., Liang, S.-L. L., Grady, M. S., & Cohen, A. S. (2005). Regional hippocampal alteration associated with cognitive deficit following experimental brain injury: A systems, network and cellular evaluation. *Neuroscience*, *133*(1), 1–15. https://doi.org/10.1016/j.neuroscience.2005.01.052

Wittner, L., Henze, D. A., Záborszky, L., & Buzsáki, G. (2007). Three-dimensional reconstruction of the axon arbor of a CA3 pyramidal cell recorded and filled in vivo. *Brain Structure and Function*, *212*(1), 75–83. https://doi.org/10.1007/s00429-007-0148-y

Woodson, W., Nitecka, L., & Ben-Ari, Y. (1989). Organization of the GABAergic system in the rat hippocampal formation: A quantitative immunocytochemical study. *Journal of Comparative Neurology*, *280*(2), 254–271. https://doi.org/10.1002/cne.902800207

Zenke, F., Gerstner, W., & Ganguli, S. (2017). The temporal paradox of Hebbian learning and homeostatic plasticity. *Current Opinion in Neurobiology*, *43*, 166–176. https://doi.org/10.1016/j.conb.2017.03.015

Zhang, L., Rzigalinski, B. A., Ellis, E. F., & Satin, L. S. (1996). Reduction of voltage-dependent Mg2+ blockade of NMDA current in mechanically injured neurons. *Science (New York, N.Y.)*, *274*(5294), 1921–1923. https://doi.org/10.1126/SCIENCE.274.5294.1921

SUPPORTING INFORMATION

Additional supporting information may be found in the online version of the article at the publisher's website.

How to cite this article: Schumm, S. N., Gabrieli, D., & Meaney, D. F. (2022). Plasticity impairment exposes CA3 vulnerability in a hippocampal network model of mild traumatic brain injury. *Hippocampus*, *32*(3), 231–250. https://doi.org/10.1002/hipo.23402